NASA TECHNICAL NOTE

NASA TN D-4911

C.1

NASA TN D-4911

HEAT-TRANSFER AND PRESSURE DISTRIBUTIONS INSIDE THE HINGE-LINE GAP OF A WEDGE-FLAP COMBINATION AT MACH NUMBER 10.4

by J. David Dearing and H. Harris Hamilton

Langley Research Center
Langley Station, Hampton, Va.

NATIONAL AERONAUTICS AND SPACE ADMINISTRATION • WASHINGTON, D. C. • NOVEMBER 1968

NASA TN D-4911

HEAT-TRANSFER AND PRESSURE DISTRIBUTIONS INSIDE THE HINGE-LINE GAP OF A WEDGE-FLAP COMBINATION AT MACH NUMBER 10.4

By J. David Dearing and H. Harris Hamilton

Langley Research Center
Langley Station, Hampton, Va.

NATIONAL AERONAUTICS AND SPACE ADMINISTRATION

For sale by the Clearinghouse for Federal Scientific and Technical Information
Springfield, Virginia 22151 – CFSTI price $3.00

HEAT-TRANSFER AND PRESSURE DISTRIBUTIONS INSIDE THE HINGE-LINE GAP OF A WEDGE-FLAP COMBINATION AT MACH NUMBER 10.4

By J. David Dearing and H. Harris Hamilton
Langley Research Center

SUMMARY

Aerodynamic heating inside the gap separating a control flap from the adjacent support structure has been measured at a nominal free-stream Mach number of 10.4. The model, a 10-percent-thick wedge, was fitted with a simple flap whose chord was 20 percent of the wedge chord. Angle of attack was varied to change the entrance-to-exit pressure ratio and resulted in local Mach numbers ahead of the gap entrance of from 5.9 to 7.9. Laminar, transitional, and turbulent boundary layers on the wedge near the entrance were obtained by combined variations in local Mach numbers and local Reynolds number.

The heating in the gap always decreased from entrance to exit and at the gap center never exceeded one-half that on the wedge at the entrance. In general, the gap heating increased with gap width and flap deflection, and rounding the gap entrance and exit lip tended to increase the overall level of heating in the gap over that for the sharp-lip configuration.

INTRODUCTION

Aerospace vehicles with flap-type controls experience severe localized heating when these controls are deflected into the stream. Heating problems also arise in the area of the flap hinge line where high temperature air passes through the gap between the flap and body. Since the gap would be of narrow-passage geometry, dissipation of heat by radiation would be small, and even with relatively small convective heating the wall temperatures in the gap might become high.

An experimental investigation of this heating problem has been conducted in the Langley continuous-flow hypersonic tunnel. Results of the initial phase of this investigation were reported earlier (ref. 1) and were concerned with the effects of the gap between the movable control and the adjacent stationary structure on the external heating. The

present report is restricted to the study of heating within the gap. This investigation used a sharp wedge with a trailing-edge flap, whose chord was approximately 20 percent of the wedge chord, located far enough from the leading edge to avoid impingement of the bow shock on the flap for all conditions tested. The heating within such a gap has also been investigated in reference 2 by using a blunt leading-edge, delta-wing configuration with a trailing-edge flap.

The current investigation was made at a nominal free-stream Mach number of 10.4 and at free-stream Reynolds numbers based on distance from the leading edge to the hinge line of 0.8×10^6 and 3.6×10^6. Angle of attack was varied from 6.83° to 12.83° to increase the entrance-to-exit pressure ratio across the gap and resulted in local Mach numbers near the gap entrance from 5.9 to 7.9. The flap was deflected from 0° to 30° in increments of 10°, and gap-center width was varied from 1/16 to 1/2 inch (0.159 to 1.27 cm) with both a sharp and rounded lip at the gap entrance and exit. Tests were also conducted with the smallest gap sealed.

SYMBOLS

The units for the physical quantities defined in this report are given in both the U.S. Customary Units and the International System of Units (SI). Factors relating these two systems of units can be found in reference 3.

A	entrance width for sharp-lip gap entrance (see fig. 2)
B	entrance width for rounded-lip gap entrance (see fig. 2)
c_p	specific heat of test gas at constant pressure
c_w	specific heat of wall material
h	heat-transfer coefficient, $\frac{q_w}{T_{aw} - T_w}$
L	surface distance from leading edge to hinge line, 23.71 inches (60.22 centimeters)
M	Mach number
N_{St}	Stanton number, $\frac{h}{\rho U c_p}$
p	pressure

q	rate of heat transfer per unit area
r_1	flap leading-edge radius, 1.202 inches (3.053 centimeters)
r_2	cove-surface radius, 1.450 inches (3.683 centimeters)
R	unit Reynolds number, $\frac{\rho U}{\mu}$
$R_{\infty,L}$	free-stream Reynolds number based on surface distance to hinge line, $\frac{\rho_\infty U_\infty L}{\mu_\infty}$
$R_{l,L}$	local Reynolds number based on surface distance to hinge line, $\frac{\rho_l U_l L}{\mu_l}$
s	surface distance from the gap entrance (see fig. 3)
T	temperature
t	time
U	velocity
x	longitudinal surface distance from the leading edge
y	lateral distance from model center line
α	angle of attack (measured from lower, instrumented surface, see fig. 1)
δ_f	flap deflection angle (see fig. 1)
ϵ	gap center width, at $\theta = 0^o$ (see fig. 2)
θ	angular distance from gap center to instrument (see fig. 3)
λ_w	model wall thickness
μ	fluid dynamic viscosity
ρ	density

Subscripts:

aw	adiabatic wall
l	local
t	total
w	wall
∞	free stream

APPARATUS, METHODS, AND TESTS

Tunnel and Injection Strut

The Langley continuous-flow hypersonic tunnel operates as a closed loop through a series of compressors with air as the test gas. The air is preheated to a stagnation temperature above 1300° F (978° K) to avoid liquefaction after expansion through the nozzle. A free-stream Mach number calibration for this facility is given in reference 1.

Prior to each test, the model was positioned in an injection chamber mounted on the side of the tunnel and was cooled to approximately 100° F (311° K) by high-pressure air jets. After the proper flow conditions were established in the test section, the model was rapidly injected into the hypersonic air stream and the data were automatically recorded. A more detailed description of the tunnel and injection strut can be found in references 1 and 4.

Model and Instrumentation

The model used in the tests was a 29.71-in-long (75.46 cm) wedge-flap combination with a ratio of trailing-edge thickness to model chord of approximately 0.1. (See fig. 1.) The leading-edge thickness was approximately 0.001 in. (0.0025 cm). For approximately 0.125 in. (0.3175 cm) downstream of the leading edge the included angle between the wedge surfaces was approximately 20° (see insert, fig. 1); however, the instrumented surface was straight, with the break occurring on the uninstrumented side. This increased effective thickness near the leading edge was necessary to prevent thermal distortion. The sides of the wedge model were swept inward toward the trailing edge at the nominal free-stream Mach angle to minimize the base area. A 6.00-in-square (15.24 cm) flap was located at the trailing edge of the model with a gap between the wedge and flap (fig. 2). The flap could be deflected through an angle of 30°. End plates were placed on each side of the flap and extended from 7.00 in. (17.78 cm) ahead of the hinge line to the trailing

edge (fig. 1). These end plates were so placed as to prevent disturbances from feeding inboard onto the flap and to reduce, or prevent, lateral flow on the flap and/or lateral outbleeding of separation regions. The support strut was attached to the side of the model for injection through the side wall of the tunnel test section. A brief series of oil-flow tests established that, in the region of the instrumentation, the flow was parallel to the model center line.

Gap size was changed by removing a section of the wedge surface ahead of the gap so that the movable section, which forms the cove surface (figs. 1 and 2), could be moved forward or aft to increase or decrease the gap width in the chordal plane. Gap widths of 1/16, 1/8, 1/4, and 1/2 in. (0.16, 0.32, 0.64, and 1.27 cm) were tested. In addition, the sharp-lip movable section was replaced by another section with a rounded lip, as shown in figure 3, to determine the effect of entrance-lip geometry on the heat transfer inside the gap. A seal was attached on the uninstrumented side of the model (fig. 2) for some tests to prevent flow through the gap. Since the cove radius was 1/4 in. greater than the flap leading-edge radius (in the gap), the gap had a constant width at the 1/4-in. setting only; for smaller gap widths, the minimum area occurs at the center and gradually increases symmetrically toward the entrance and exit. Larger gaps had the reverse area change, with area at the center being greatest and decreasing symmetrically toward entrance and exit. Dimensions of the gaps are tabulated in figure 2.

Pressure orifices were installed along the flap surface inside the gap (fig. 3 and table 1). Each pressure orifice in the gap was connected to either a strain-gage pressure transducer with range from 0 to 1 psi (0 to 6.89 kN/m^2), 0 to 3 psi (0 to 20.7 kN/m^2), or to an ionization pressure gage with range from 0 to 0.6 psi (0 to 4.1 kN/m^2). The manufacturers' stated accuracy for these instruments is ± 0.25 percent of full scale for the pressure transducers, and ± 5 percent of the measured pressure below 0.02 psi (0.14 kN/m^2) and ± 2 percent of the measured pressure from 0.02 to 0.6 psi (0.14 to 4.1 kN/m^2) for the ionization pressure gages. The outputs from the pressure instruments were recorded on magnetic tape by a high-speed, analog-to-digital data recording system. In order to increase the accuracy of the pressure transducers, their measured pressures, while still in the low pressure environment of the injection chamber, were compared and adjusted to agree with those of the more accurate ionization gages. This method resulted in better accuracy than that obtained with only the pretest calibrations. All pressures presented herein were recorded after steady-state conditions were reached on the model.

Temperatures of the model surface were measured by chromel-alumel thermocouples located on either side of the center line of the lower wedge and flap surfaces (fig. 1) and on both the cove and flap surfaces in the gap (fig. 3 and table 1). Individual temperatures were recorded simultaneously with the pressures at intervals of 0.05 second.

Tests

Tests were conducted at stagnation pressures of 300 and 1500 psia (2.1 and 10.3 MN/m^2). The test stream conditions, calculated using real-gas relations, for these stagnation pressures are presented in the following table:

p_t		T_t		M_∞	p_∞		T_∞		R_∞	
psia	MN/m^2	^oR	^oK		psia	N/m^2	^oR	^oK	per foot	per meter
300	2.1	1760	978	10.18	6.0×10^{-3}	41.8	84.2	46.8	0.41×10^6	1.35×10^6
1500	10.3	1840	1022	10.48	25.5×10^{-3}	175.9	84.2	46.8	1.79×10^6	5.87×10^6

The configurations tested and for which the data are presented are listed in the following table:

p_t		α, deg	δ_f, deg	ϵ/r_1	Figure	
psia	MN/m^2				Sharp entrance	Rounded entrance
300	2.1	6.83	0 10 20	Sealed (0.052)	5 and 8	
		6.83	0 10 20	0.052	6 and 8	
		6.83	0 10 20	0.208	7 and 8	
1500	10.3	6.83	0 10 20 30	Sealed (0.052)	9 and 13	
		6.83	0 10 20 30	0.052	10 and 13	16
		6.83	0 10 20 30	0.104	11 and 13	
		6.83	0 10 20 30	0.208	12 and 13	17
		6.83	0 10 20 30	0.416		18
1500	10.3	12.83	0 10 20	0.052	14	19
		12.83	0 10 20	0.208	15	20

The local Mach number ahead of the gap entrance for $\alpha = 6.83^{\circ}$ was 7.7 for the lower stagnation pressure and 7.9 for the higher. At $\alpha = 12.83^{\circ}$ the local Mach number was 5.9. The local Mach numbers were taken from reference 5 for an ideal-gas, inviscid, oblique-shock system.

Tunnel blockage prevented testing at the lower stagnation pressure with $\delta_f > 20^{\circ}$ and at the higher pressure with $\alpha = 12.83^{\circ}$ and $\delta_f > 20^{\circ}$.

Reduction of Heat-Transfer Data

The heat transfer was determined by the transient calorimeter technique using the recorded temperature time histories in the following equation:

$$q = h\left(T_{aw} - T_w\right) = \rho_w \lambda_w c_w \frac{dT_w}{dt}$$

The derivative in this equation was determined at the center of a 4-second time interval of recorded data from a least-squares, second-degree polynomial curve fitted to the data. The density of the inconel wall ρ_w was taken (from ref. 6) to be 528.4 lbm/ft^3 (8465 kg/m^3) and the specific heat was determined from a straight-line curve fit of the data in reference 6. The wall thickness λ_w was 0.03 inch (0.076 cm). The adiabatic wall temperature T_{aw} inside the gap was assumed to be equal to the stagnation temperature.

Several attempts were made to obtain an estimate of the surface conduction inside the gap. Because of the small temperature changes and heating rates, an accurate estimate could not be obtained; but the values which were obtained indicated that the heating distributions would not change significantly if corrected for conduction, and hence, no conduction correction has been applied to the data.

The data measurement and reduction system used has a maximum sensitivity to temperature changes of $\pm 0.304^{\circ}$ for the Fahrenheit scale ($\pm 0.169^{\circ}$ for the Kelvin scale), which over the 4-sec data reduction interval results in an uncertainty in $N_{St,\infty}\sqrt{R_{\infty,L}}$ of ± 0.076 in the individual points at the lower stagnation pressure and ± 0.032 at the higher pressure; however, the slope of the temperature with time was obtained from a least-squares curve fit to the recorded data which, because it takes into account all data points in the interval, was able to resolve much smaller slopes than would be expected from considerations of the data-system sensitivity. The exact limit of resolution cannot be accurately defined but the heat-transfer data show little scatter down to approximately $N_{St,\infty}\sqrt{R_{\infty,L}}$ of 0.010 at the lower stagnation pressure and 0.005 at the higher pressure. The data in the region below these limits (shown cross hatched in the figures) are questionable and, though presented for completeness, have not been considered in the fairing of the data.

RESULTS AND DISCUSSION

External Flow

In figure 4, heat-transfer distributions are presented from reference 1 for the external flow with zero flap deflection. These distributions indicate that at the lower Reynolds number (fig. 4(a)) the boundary layer over the entire model was laminar. At the higher Reynolds number, the external boundary layer at the hinge line was transitional for $\alpha = 6.83^{\circ}$ (fig. 4(b)), and turbulent for $\alpha = 12.83^{\circ}$ (fig. 4(c)).

In the laminar regime, deflection of the flap resulted in separation of the boundary layer upstream of the gap entrance for most gap sizes. A simplified sketch of a typical flow pattern over the wedge-flap at the lower free-stream Reynolds number with the gap open is as follows:

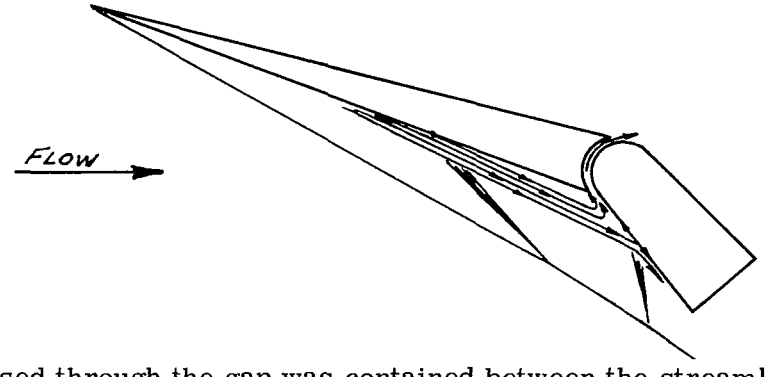

The mass that passed through the gap was contained between the streamline defining the recirculation region and the "dividing streamline" that reattaches to the flap. Generally, increasing the gap width was found to decrease the extent of the separation; however, separation was always present except for the case where $\epsilon/r_1 = 0.208$ and $\delta_f = 10^{\circ}$.

At the higher free-stream Reynolds number, the boundary layer remained attached to the wedge surface for all combinations of flap deflection and gap size tested. The flow pattern for these conditions with an open gap is shown in the following simplified sketch:

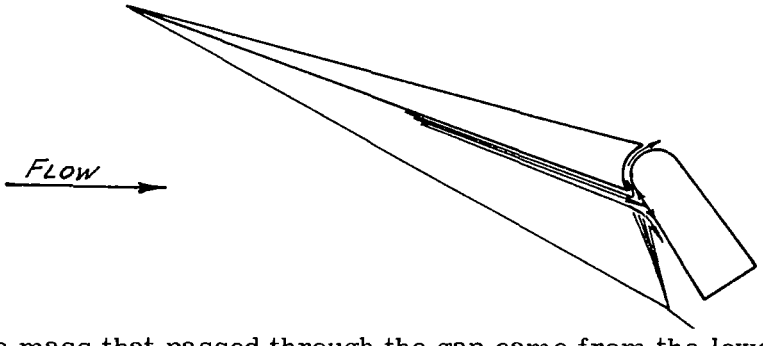

In this case, the mass that passed through the gap came from the lower-energy portion of the external boundary layer. Increasing gap width had only a slight effect on the external flow.

Internal Flow

Pressure ratios $\frac{p}{p_\infty}$ and heat-transfer parameter $N_{St,\infty}\sqrt{R_{\infty,L}}$ distributions from the various gaps and external flows are presented in figures 5 to 20 as functions of θ, the angular distance in the gap, measured from the plane of symmetry of the wedge as shown in figure 3. The vertical lines in each figure indicate the entrance and exit of the gap. The horizontal line (marked reference heating) indicates the level of heating on the wedge surface, just ahead of the gap entrance lip (at the reference heating point shown in fig. 3) taken from reference 1. The arrow on the pressure plots indicates the reference wedge pressure (at the reference heating point). The crosshatched area at the bottom of each figure represents the region in which the reliability of the data is uncertain (because of low accuracy) as discussed previously.

Laminar external flow.- Data for the sealed, sharp-entrance gap $\left(\epsilon/r_1 = 0.052\right)$ with $R_{\infty,L} = 0.8 \times 10^6$ are presented in figure 5. The angle of attack was 6.83°, the local Reynolds number $R_{l,L}$ was 1.18×10^6, and the local Mach number M_l was 7.7.

For $\delta_f = 0°$ (fig. 5(a)), the pressure is very nearly constant from entrance to exit in the gap and is approximately equal to the pressure on the wedge at the entrance. Increasing δ_f to 10° and 20° results in separation of the external boundary layer ahead of the gap entrance, and the pressure inside the gap increases to the corresponding plateau pressure of the separated region and remains constant through the gap.

The gap heating under the conditions of no gap flow is greatest at the entrance and decreases rapidly through the gap. At the lower flap deflections, heating within the gap was very small (generally below the resolution limit); however, at $\delta_f = 20°$ the gap heating was significantly higher than at the lower flap deflections.

The heating to the cove and flap surfaces is approximately the same at equal values of θ for both rows of thermocouples; thus, these data have been faired as one curve.

Opening the gap produces a favorable pressure gradient within the gap. The pressure outside the exit is nearly constant for all conditions, whereas the entrance pressure increases with flap deflection. At $\delta_f = 0°$ (fig. 6(a)), the heating parameter $N_{St,\infty}\sqrt{R_{\infty,L}}$ in the gap decreases rapidly from the reference value to 0.01 and remains low through the remainder of the gap. The increase in heating to the cove surface near the exit is probably due to conduction. It was impossible to determine the magnitude of conduction near the entrance and exit lips of the cove surface because of the geometry of the model and sparsity of instrumentation. For this reason, no conduction correction is made, and the increase in heating is not considered in the fairings. Deflecting the flap to 10° (fig. 6(b)) produces a slight increase in the gap heating. For $\delta_f = 20°$ (fig. 6(c)) the heating throughout the forward half of the gap has increased. The heat-transfer parameter in the

gap still decreases to less than 0.01. However, the point at which this occurs is nearer the gap exit ($\theta > 0^o$).

For the larger gap at $\delta_f = 0^o$ (fig. 7(a)), the heating to the flap surface outside the entrance was 30 percent higher than at the reference heating point. At the entrance, the heating has decreased by a factor of 3 and continues to decrease through the gap except on the cove surface near the exit. For $\delta_f = 10^o$ and 20^o (figs. 7(b) and 7(c)) the heating in the gap still decreases from entrance to exit, but the overall magnitude of the heating has greatly increased. For this gap width $\epsilon/r_1 = 0.208$ the heating in the gap is nowhere less than 10 percent of the reference heating level for $\delta_f = 10^o$ and 20 percent for $\delta_f = 20^o$.

The pressure and heat-transfer distributions from the open-gap tests (figs. 6 and 7) are superimposed on the sealed-gap results in figure 8. The short vertical marks indicate the entrance and exit of the gaps as before. The short horizontal lines on the vertical axis of each plot indicate the respective reference heating levels. The pressure gradients within the larger gap $(\epsilon/r_1 = 0.208)$ are smaller than for the smaller gap $(\epsilon/r_1 = 0.052)$. The differences in the distributions can be explained, in part, by the differences in gap geometry. The smaller gap had a varying cross section, with the minimum area at the gap center ($\theta = 0^o$) and maximum areas at the entrance and exit. The larger gap had a constant cross-sectional area, and thus boundary-layer growth through the gap probably caused the minimum effective area to occur at the exit.

In general, the heating in the gap increases with increasing gap size and flap deflection, perhaps because more mass may flow through the larger gap and at the higher flap deflections. A greater increase in the heating occurs when gap size increases from $\epsilon/r_1 = 0.052$ to 0.208 than when the seal is removed from the smaller gap. For the larger gap with $\delta_f = 20^o$, the heating in the gap is nowhere less than 20 percent of that on the wedge surface ahead of the hinge line. However, since the net effect of radiation on surface cooling within the gap is probably small, equilibrium gap-surface temperatures might present a problem if the heating continued over an extended period.

Transitional external flow.- The pressure and heat-transfer distributions inside the sealed, sharp-entrance gap with the wedge boundary layer transitional at the gap entrance are shown in figure 9. The free-stream Reynolds number $R_{\infty,L}$ was 3.6×10^6, the angle of attack was 6.83^o, the local Reynolds number $R_{\ell,L}$ was 5.3×10^6, and the local Mach number was 7.9.

The pressure in the gap was approximately constant and slightly lower than the pressure on the flap surface ahead of the gap entrance. The heat-transfer parameter $N_{St,\infty}\sqrt{R_{\infty,L}}$ at the reference heating point for this set of data is much higher than for the lower Reynolds number because the external boundary layer is now transitional. The pressure and heat-transfer distributions inside the gap are similar to those for the lower

Reynolds number. Care should be exercised in comparing the relative magnitudes of the heat-transfer parameter $N_{St,\infty}\sqrt{R_{\infty,L}}$ for the higher and lower Reynolds number tests since the free-stream reference quantities are different. (See the first table in the section "Tests.") Thus, equal values of $N_{St,\infty}\sqrt{R_{\infty,L}}$ at different free-stream Reynolds numbers do not indicate that the heating rates are equal.

For similar test conditions, the pressure and heat-transfer distributions in the open gap are presented in figures 10, 11, and 12 for $\epsilon/r_1 = 0.052$, 0.104, and 0.208, respectively. At this Reynolds number, even the largest flap deflection tested $(\delta_f = 30^o)$ did not produce measurable separation. The pressure distributions inside the gap are similar to those at the lower Reynolds number, but local values of p/p_∞ are generally lower because the external flow did not separate.

The fact that the exterior flow is transitional causes the heat-transfer parameter at the gap entrance to be greater at this Reynolds number than at the lower Reynolds number where the external boundary layer was laminar (figs. 6 and 7). The heating still decreases rapidly through the gap as it did at the lower Reynolds number. As flap deflection increases, the heating in the gap also increases.

The effect of gap width with a transitional boundary layer ahead of the gap entrance can be ascertained from figure 13, where the fairings of figures 10, 11, and 12 are superimposed upon those for the sealed gap (fig. 9). In general, heating in the gap increases with gap size and flap deflection as was the case at the lower Reynolds number. However, from the entrance to $\theta = 0^o$ (gap center) the changes produced by increasing gap size are, generally, smaller than those from $\theta = 0^o$ to the exit. The reduction in heating achieved by sealing the smallest gap $(\epsilon/r_1 = 0.052)$ is of the same order of magnitude as that which results from reducing the gap size from $\epsilon/r_1 = 0.208$ to $\epsilon/r_1 = 0.052$.

Turbulent external flow.- Increasing the angle of attack to 12.83° caused the external boundary layer to become turbulent at the gap entrance. The local Reynolds number $R_{l,L}$ and Mach number M_l were approximately 4.5×10^6 and 5.9, respectively. The entrance-to-exit pressure ratio across the gap was also much higher than at the lower angle of attack, and the flow through the gap was probably choked for both cases. Data for the sharp-entrance gaps with $\epsilon/r_1 = 0.052$ and 0.208 are presented in figures 14 and 15, respectively. The dashed curves in these figures are the fairings of the data for the same gap size, entrance configuration, and free-stream conditions at the lower angle of attack ($\alpha = 6.83^o$).

The pressure on the wedge surface outside the entrance is much higher at the higher angle of attack but, inside the gap, the pressures are approximately the same as for the lower angle of attack (except for the smaller gap with $\delta_f = 0^o$). Because of the higher local pressure on the windward surface and the fact that the boundary layer is turbulent, the reference heating is also higher. Inside the smaller gap (fig. 14), the heating is also

higher for the higher angle of attack, but the difference diminishes as flap deflection increases.

For the larger gap (fig. 15), at the higher angle of attack, flap deflection appears to have little effect on either the pressure or heat transfer inside the gap. This differs from the results at the lower angle of attack (dashed curves), where increasing the flap deflection is accompanied by an increase in the local heat transfer inside the gap.

Effect of rounding the gap-entrance lip.- The rounded-entrance configuration (shown in figs. 2 and 3(b)) was tested with three gap sizes at both angles of attack and $R_{\infty,L} = 3.6 \times 10^6$. The reference heating point was chosen at a point slightly farther from the hinge line for this configuration (fig. 3(b)) to avoid the influence of the rounded lip. The pressure and heat-transfer distributions for this gap-entrance configuration are presented in figures 16, 17, and 18 for $\alpha = 6.83^\circ$ and figures 19 and 20 for $\alpha = 12.83^\circ$. The dashed curves represent the pressure and heat-transfer distributions for the corresponding sharp-entrance gap at the same test conditions.

For $\epsilon/r_1 = 0.052$ (fig. 16), the pressure distributions for the two configurations are approximately the same for all flap deflections except $\delta_f = 10^\circ$. The heat-transfer distributions are also similar, but the heating for the rounded-entrance configuration is greater.

As gap size is increased to $\epsilon/r_1 = 0.208$ (fig. 17), the differences noted for the smaller gap diminish and for $\delta_f = 20^\circ$ completely disappear. Note that for the rounded-entrance configuration in figure 17, the heating on the cove surface tends to be slightly higher than the heating on the flap surface at the same location. For the largest gap (i.e., $\epsilon/r_1 = 0.416$, shown in fig. 18), the heating on the cove surface is much higher than the heating on the flap surface. No dashed curves for the sharp-entrance configuration are shown in figure 18 because no comparable gap size was tested for that configuration. The crosshatched bands in figure 18 are used to emphasize the difference which now exists between the heat transfer on the flap and cove surfaces in the gap.

A comparison of the pressure and heat-transfer distributions for the sharp- and rounded-entrance gaps at $R_{\infty,L} = 3.6 \times 10^6$ and $\alpha = 12.83^\circ$ $\left(R_{\ell,L} = 4.5 \times 10^6 \text{ and } M_\ell = 5.9\right)$ is presented in figures 19 and 20 for gaps with $\epsilon/r_1 = 0.052$ and 0.208, respectively. The pressure distributions for the two cases differ only slightly within the gap. For the smaller gap (fig. 19), the heat-transfer distributions are very similar for the two cases but the heat transfer in the rounded-entrance configuration is always greater, often by a factor of 3. For the larger gap (fig. 20), these trends hold; however, the differences between the heating for the two configurations are not as great as for the smaller gap. The differences between the heating on the cove and flap surfaces that were observed for the rounded-entrance gap at the lower angle of attack are now much less pronounced.

Correlation of gap heating data.- In the preceding sections, the heat transfer in the gap has been shown to be a function of a number of gap geometry and external flow variables. It is felt that some basic similarity of the gap flow should exist; therefore, a gross correlation of the data was attempted in terms of two basic parameters within the gap, local pressure and distance from the gap entrance. (See fig. 3.) To this end, all the measured gap heating results from open gaps at $\alpha = 6.83^{\circ}$ are shown in figure 21, subdivided by flap deflection angle, in terms of the parameter $\frac{N_{St,\infty}\sqrt{R_{\infty,L}}}{p/p_{\infty}}$ and the ratio of gap distance s to the gap center width ϵ. Only the flap surface heating data have been presented since the cove surface heating was, in general, the same and only tended to reduce the clarity of the figure because of the large amount of data presented.

It is found, with the use of these parameters, that for the higher Reynolds number data a gross correlation exists at any particular flap deflection. The data for the lower Reynolds number, however, do not agree with this correlation except for the larger gap $\left(\epsilon/r_1 = 0.208\right)$ at $\delta_f = 10^{\circ}$ and 20°. The correlation appears to improve as flap deflection and gap size increase or as the gap flow and gap heat-transfer rates increase.

The basic similarity of results is apparent for the decay of the heating with s/ϵ for all gaps (excluding lower Reynolds number) at each flap deflection. Most of these data are at values of s/ϵ where correlations such as those used for fully developed pipe flow would not be expected to exist. Also apparent is the decrease in the rate of decay of the heating (decreasing slope of the correlation) with increasing flap deflection as noted in the basic data. The differences between the heating in the sharp- and rounded-entrance gaps, which were pointed out previously when the heating was examined as a function of θ in the gap, are not as pronounced when the gap heating is divided by the local pressure and compared at equal s/ϵ locations.

SUMMARY OF RESULTS

Heat-transfer and pressure results have been presented for a gap ahead of a flap on a thin, sharp-leading-edge wedge. The data were obtained at a nominal free-stream Mach number of 10.4 and two free-stream Reynolds numbers based on the distance to the hinge line of 0.8×10^6 and 3.6×10^6. The tests were made with the gap sealed and with the gap open with various gap-center widths; flap deflections ranged from 0° to 30°. The angle of attack was varied to determine the effect of increasing the entrance-to-exit pressure ratio across the gap, and resulted in local Mach numbers outside the entrance of approximately 5.9 to 7.9. This range of conditions resulted in laminar, transitional, and turbulent boundary layers on the exterior wedge surfaces near the gap entrance. The laminar boundary layer was separated by most combinations of gap size and flap deflection but the transitional and turbulent boundary layers could not be separated for any combination of gap

size and flap deflection tested. With these external flows, the following heating results in the gaps were obtained:

1. For all conditions tested, heating in the gap was less than that on the wedge surface near the gap entrance (reference heating point), with the heating at the gap center never exceeding one-half that at the reference point.

2. In general, the heating in the gap increased with flap deflection and gap size and decreased with distance from the gap entrance.

3. Sealing the gap always resulted in a reduction in gap heating. When the external boundary layer was laminar, this reduction was relatively small compared with the reduction achieved by decreasing gap size by a factor of four. When the external boundary layer was transitional at the gap entrance and the heating rates in the gap were higher, the reduction achieved by sealing the gap was of the same order of magnitude as that resulting from a reduction of the gap size by a factor of 4.

4. Rounding the entrance lip of the gap tends to increase the overall level of gap heating over that for the sharp-lip configuration. For several test conditions with the rounded-lip configuration, the heating on the cove surface was as much as twice that on the flap surface inside the gap.

5. A gross correlation of the gap heating data is found to exist when the heating is divided by the local pressure and compared at equal values of the ratio of distance from the entrance to the gap width at the gap center. This correlation is found to exhibit a strong effect of flap deflection and tends to break down when the external (wedge) boundary layer is separated ahead of the entrance or whenever the gap flow is small and hence the heat-transfer rate small.

Langley Research Center,
National Aeronautics and Space Administration,
Langley Station, Hampton, Va., August 2, 1968,
129-01-07-08-23.

REFERENCES

1. Hamilton, H. Harris; and Dearing, J. David: Effect of Hinge-Line Bleed on Heat Transfer and Pressure Distribution over a Wedge-Flap Combination at Mach 10.4. NASA TN D-4686, 1968.

2. Stern, I.; and Rowe, W. H., Jr.: Effect of Gap Size on Pressure and Heating Over the Flap of a Blunt Delta Wing in Hypersonic Flow. J. Spacecraft Rockets, vol. 4, no. 1, Jan. 1967, pp. 109-114.

3. Mechtly, E. A.: The International System of Units – Physical Constants and Conversion Factors. NASA SP-7012, 1964.

4. Dunavant, James C.; and Stone, Howard W.: Effect of Roughness on Heat Transfer to Hemisphere Cylinders at Mach Numbers 10.4 and 11.4. NASA TN D-3871, 1967.

5. Dennard, John S.; and Spencer, Patricia B.: Ideal-Gas Tables for Oblique-Shock Flow Parameters in Air at Mach Numbers From 1.05 to 12.0. NASA TN D-2221, 1964.

6. Lucks, C. F.; and Deem, H. W.: Thermal Properties of Thirteen Metals. Spec. Tech. Publ. No. 227, Amer. Soc. Testing Mater., 1958.

TABLE 1.- INSTRUMENT LOCATION

Flap surface				Cove surface		
Thermocouple	θ, deg (a)	Pressure orifice	θ, deg (a)	Thermocouple	θ, deg (b)	
					Sharp lip	Rounded lip
1	-90	1	-90	1	-45.0	-44.5
2	-75	2	-60	2	-37.5	-38.5
3	-60	3	-30	3	-30.0	-30.0
4	-45	4	0	4	-15.0	-15.0
5	-30	5	30	5	0	0
6	-15	6	60	6	15.0	15.0
7	0	7	90	7	30.0	30.0
8	15			8	37.5	38.5
9	30			9	45.0	44.5
10	45					
11	60					
12	75					
13	90					

[a]Based on $\delta_f = 0^o$.

[b]Based on location for $\epsilon/r_1 = 0.208$ gap.

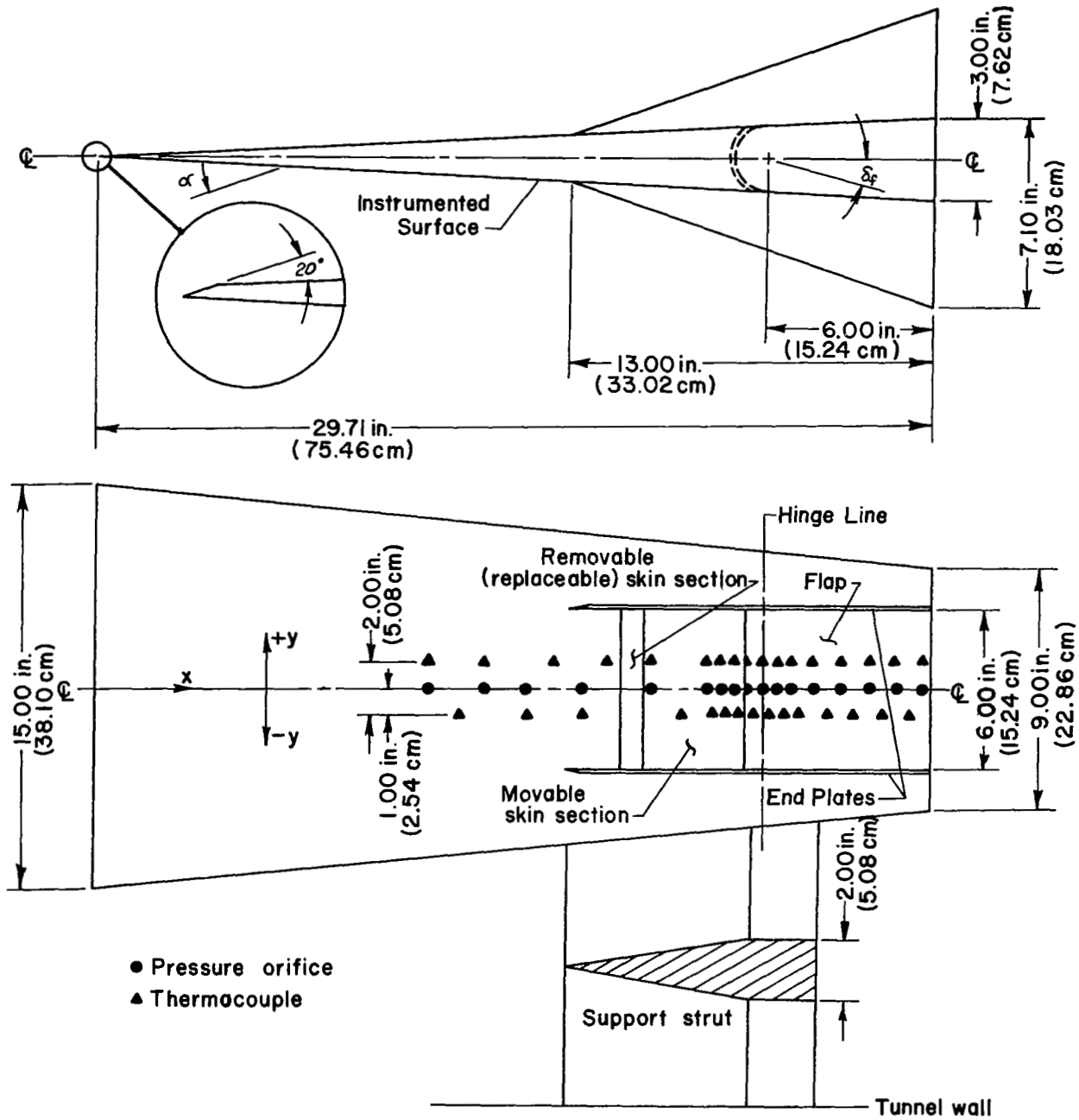

Figure 1.- Basic configuration details.

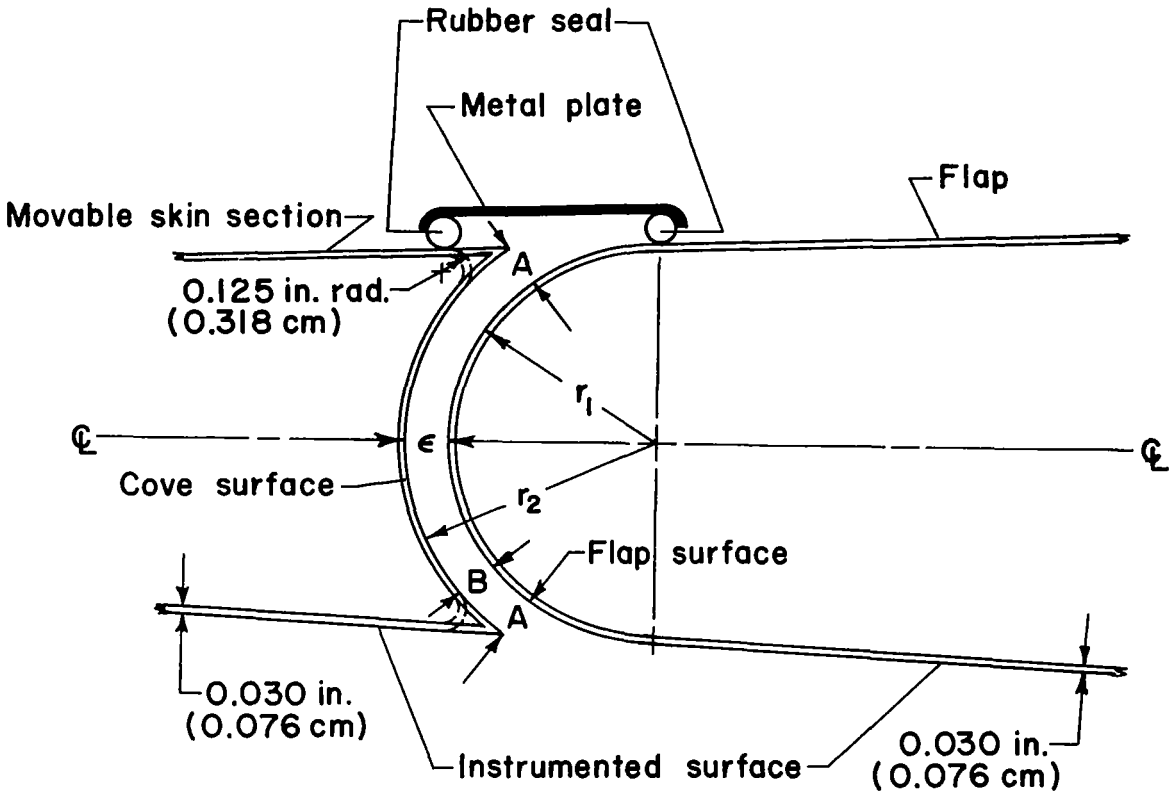

$\frac{\epsilon}{r_1}$	ϵ		A		B	
	inch	cm	inch	cm	inch	cm
0.052	0.063	0.159	0.150	0.381	0.110	0.279
0.104	0.125	0.318	0.175	0.445	-----	-----
0.208	0.250	0.635	0.250	0.635	0.250	0.635
0.416	0.500	1.270	-----	-----	0.450	1.143

r_1 = 1.202 inch (3.053 cm)

r_2 = 1.450 inch (3.683 cm)

Figure 2.- Details of gaps.

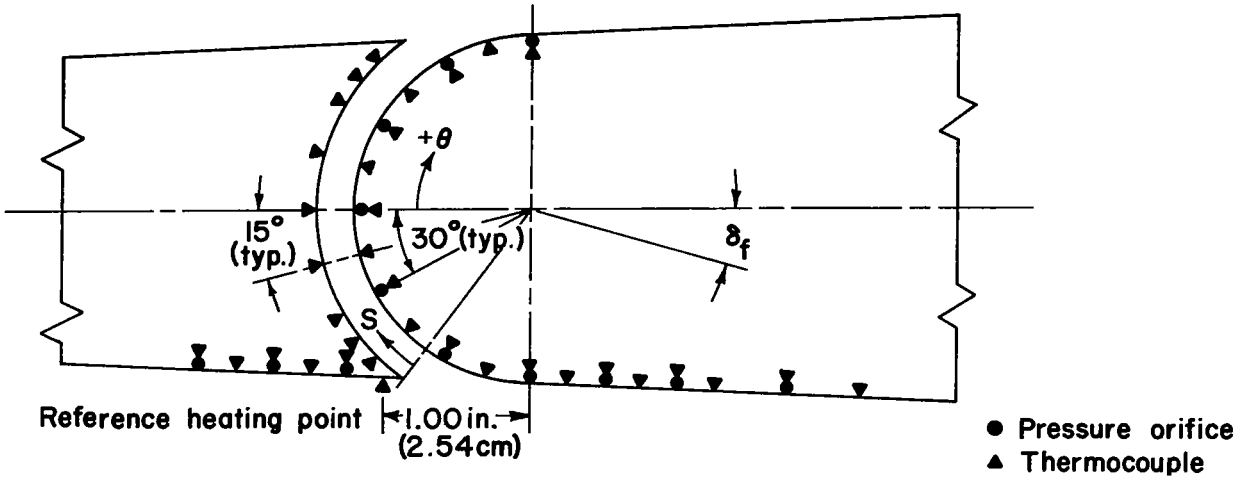

(a) Sharp entrance.

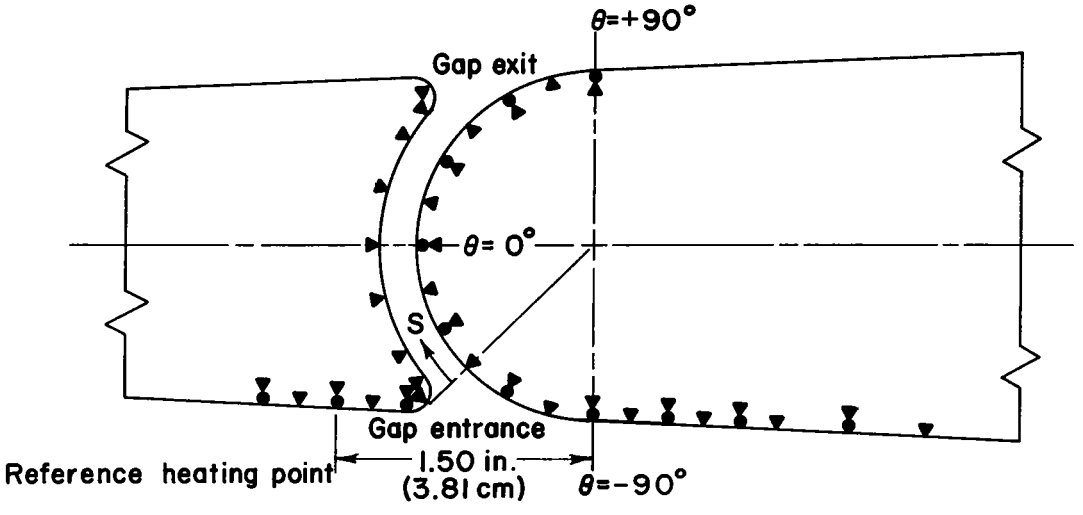

(b) Rounded entrance.

Figure 3.- Instrumentation in the gap. Linear dimensions based on gap width, ε = 0.250 in. (0.635 cm).

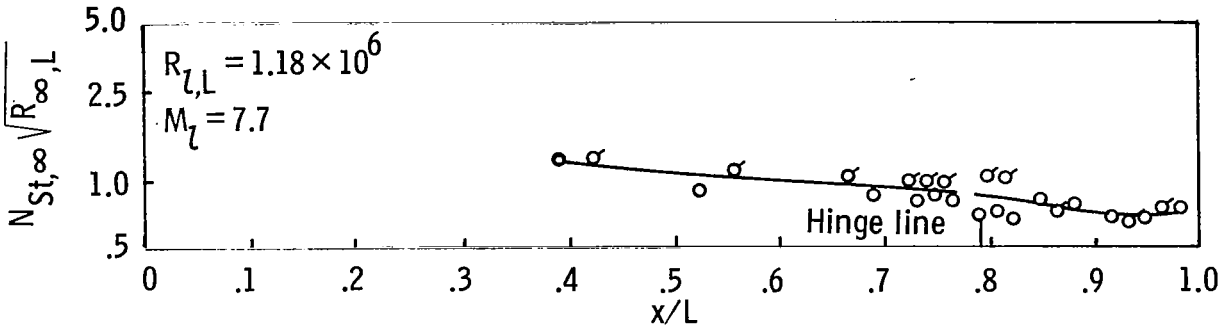

(a) $\alpha = 6.83^0$; $R_{\infty,L} = 0.8 \times 10^6$; laminar at hinge line.

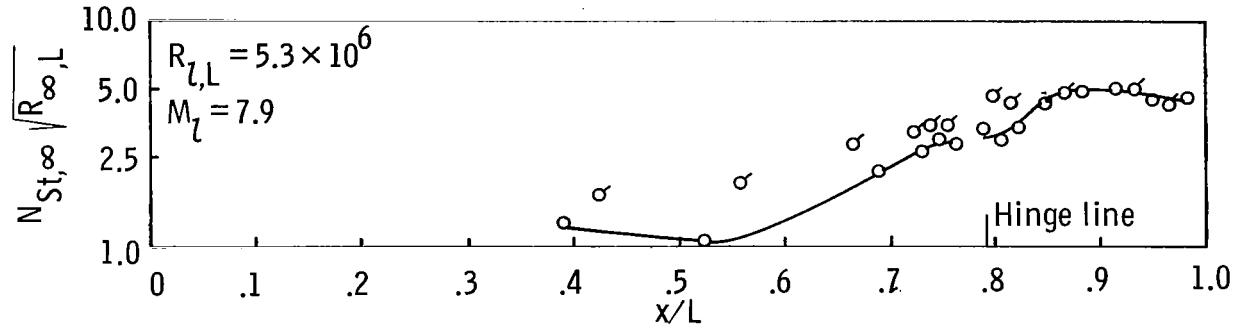

(b) $\alpha = 6.83^0$; $R_{\infty,L} = 3.6 \times 10^6$; transitional at hinge line.

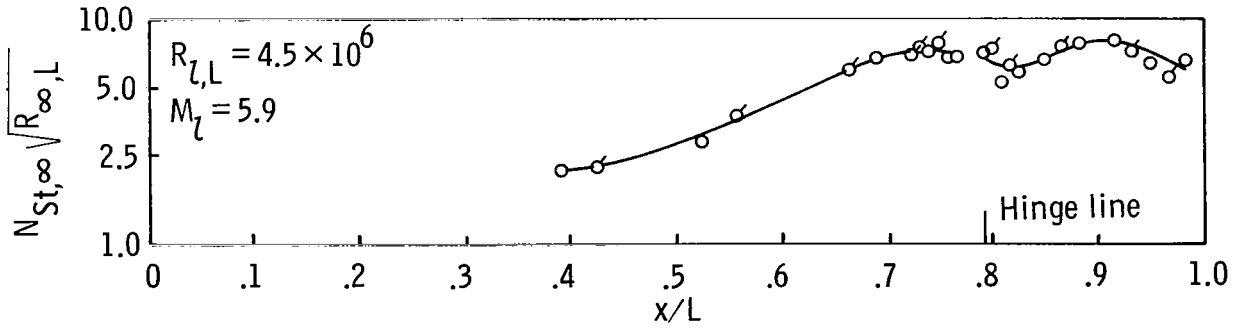

(c) $\alpha = 12.83^0$; $R_{\infty,L} = 3.6 \times 10^6$; turbulent at hinge line.

Figure 4.- Heat-transfer distributions on the wedge and flap with $\delta_f = 0^0$. Flagged symbols, -y location; unflagged symbols, +y location.

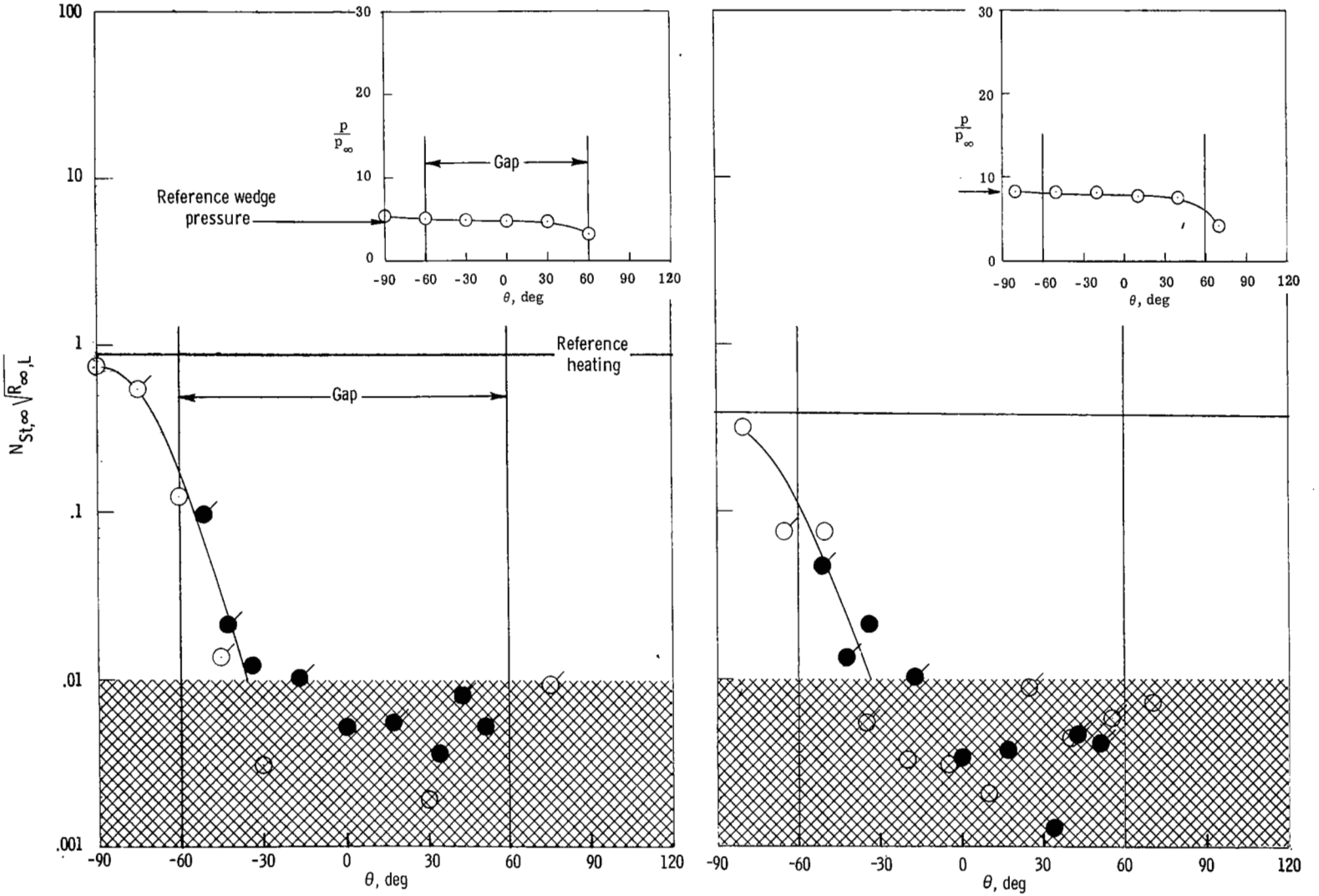

(a) $\delta_f = 0^0$.

(b) $\delta_f = 10^0$.

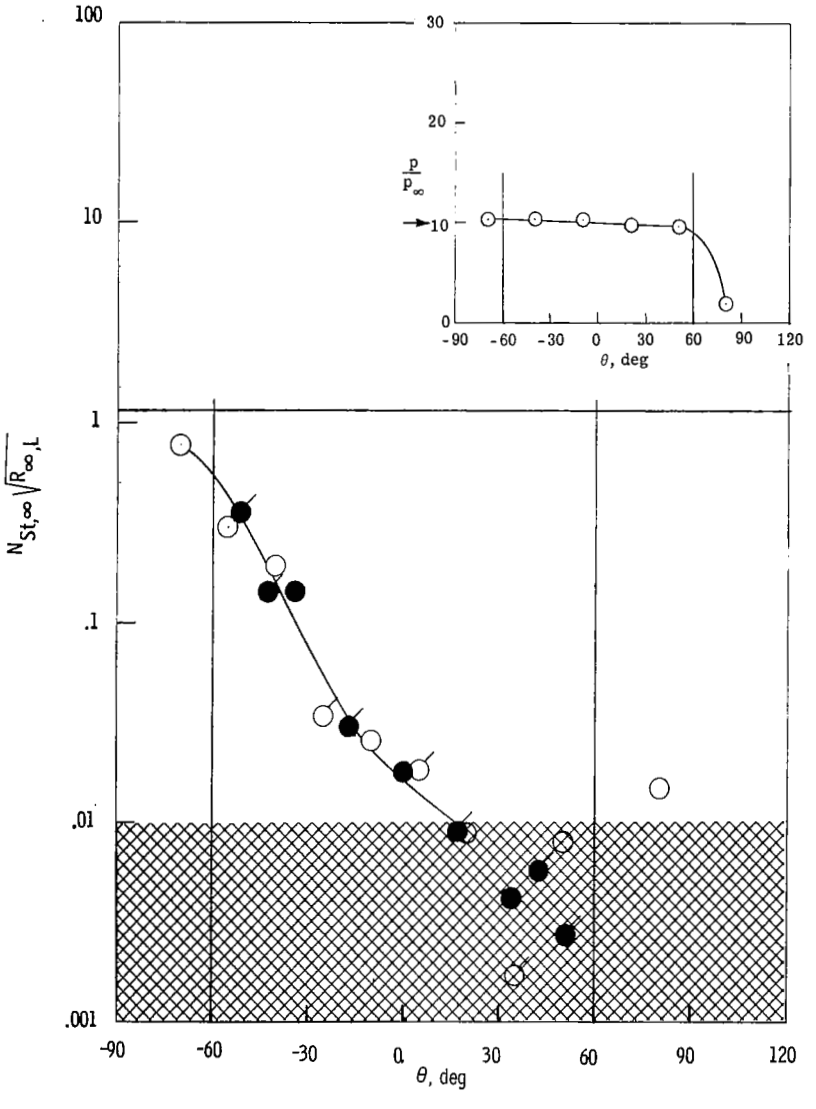

Flap surface data
Cove surface data
Flagged symbols, -y location
Unflagged symbols, +y location

(c) $\delta_f = 20^0$.

Figure 5.- Pressure and heat-transfer distributions in the sealed, sharp-entrance gap for $\varepsilon/r_1 = 0.052$, $R_{\infty,L} = 0.8 \times 10^6$, and $\alpha = 6.83^0$. $R_{l,L} = 1.18 \times 10^6$; $M_l = 7.7$.

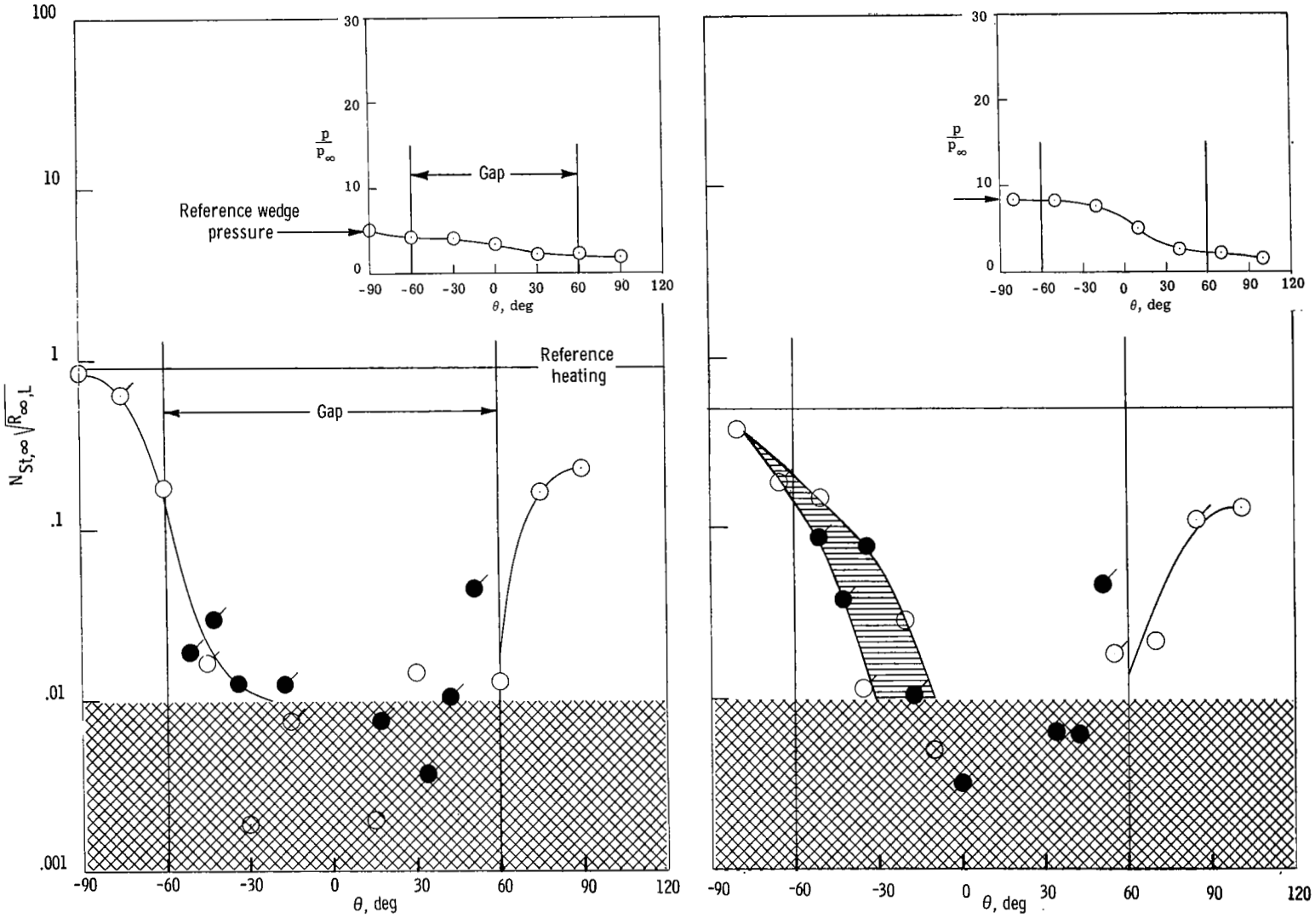

(a) $\delta_f = 0^o$.

(b) $\delta_f = 10^o$.

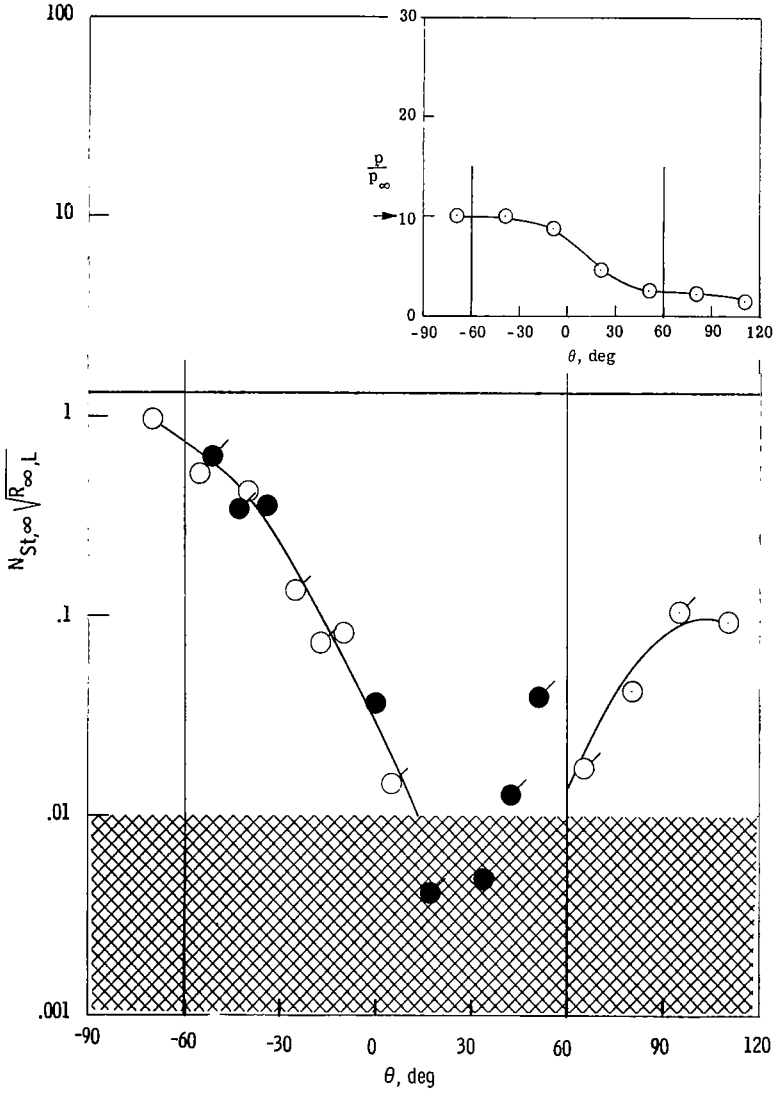

○ Flap surface data
● Cove surface data
Flagged symbols, -y location
Unflagged symbols, +y location

(c) $\delta_f = 20^0$.

Figure 6.- Pressure and heat-transfer distributions in the open, sharp-entrance gap for $\varepsilon/r_l = 0.052$, $R_{\infty,L} = 0.8 \times 10^6$, and $\alpha = 6.83^0$. $R_{l,L} = 1.18 \times 10^6$; $M_l = 7.7$.

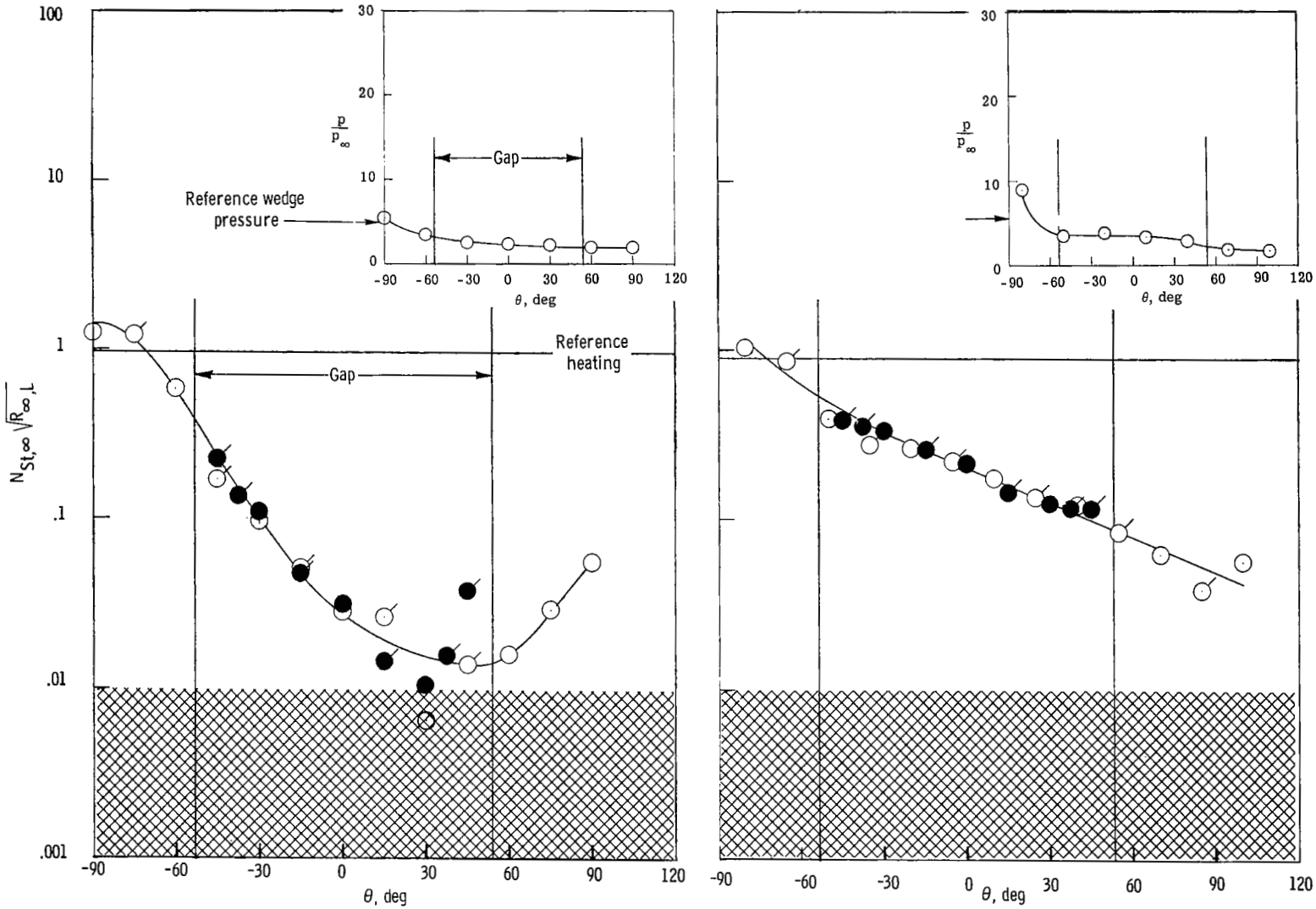

(a) $\delta_f = 0^0$.

(b) $\delta_f = 10^0$.

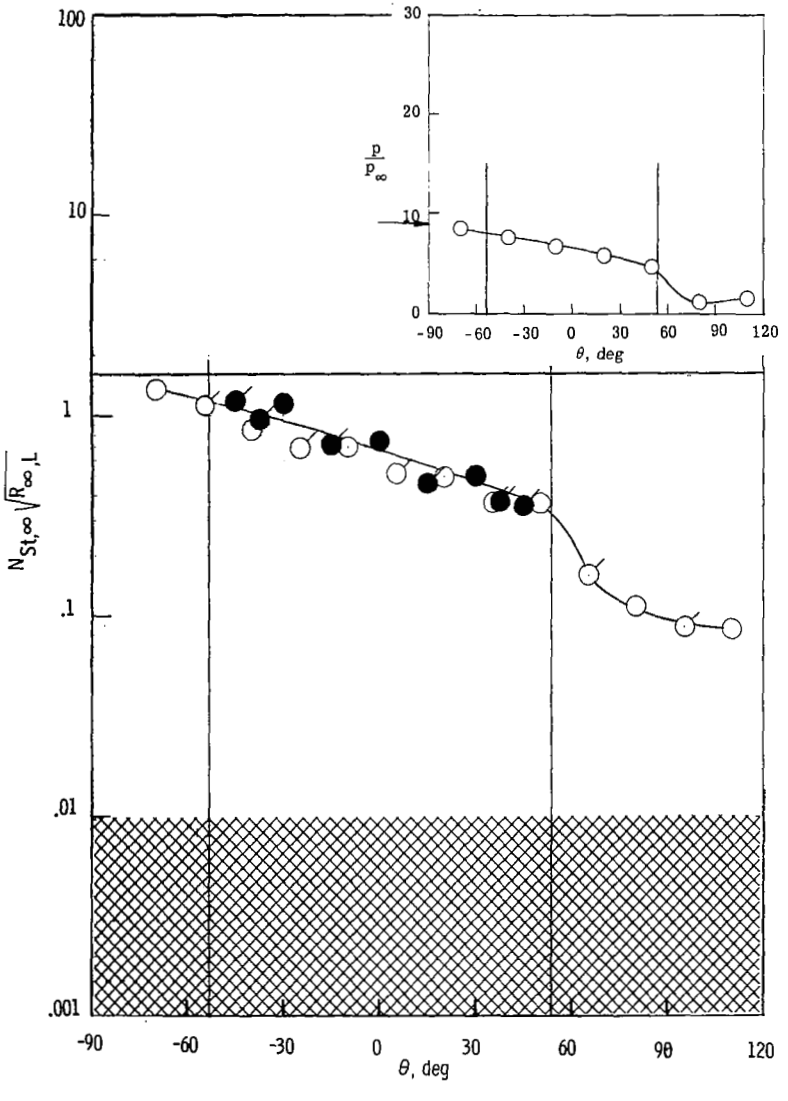

Flap surface data
Cove surface data
Flagged symbols, -y location
Unflagged symbols, +y location

(c) $\delta_f = 20^0$.

Figure 7.- Pressure and heat-transfer distributions in the open, sharp-entrance gap for $\varepsilon/r_l = 0.208$, $R_{\infty,L} = 0.8 \times 10^6$, and $\alpha = 6.83^0$. $R_{l,L} = 1.18 \times 10^6$; $M_l = 7.7$.

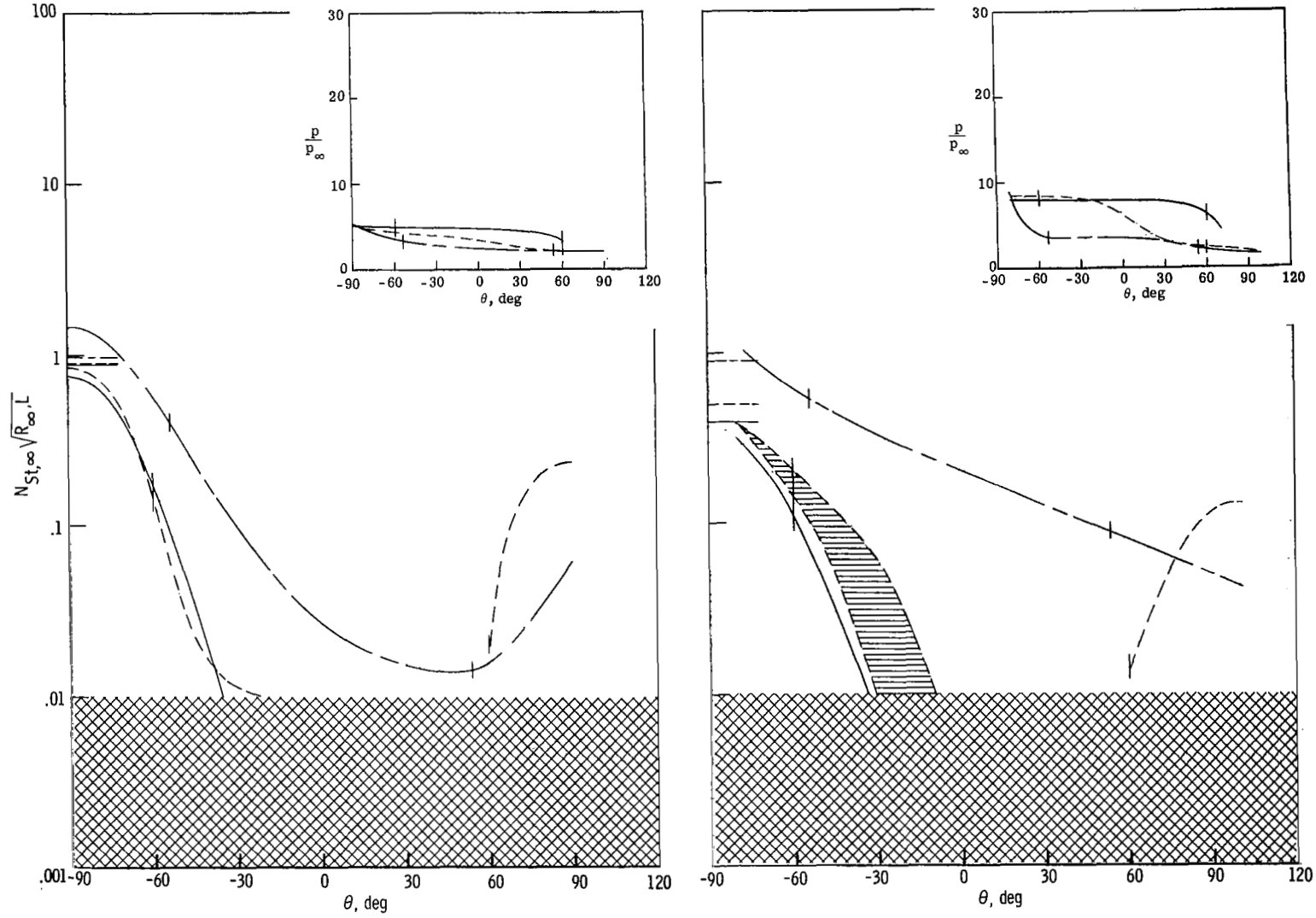

(a) $\delta_f = 0^o$.

(b) $\delta_f = 10^o$.

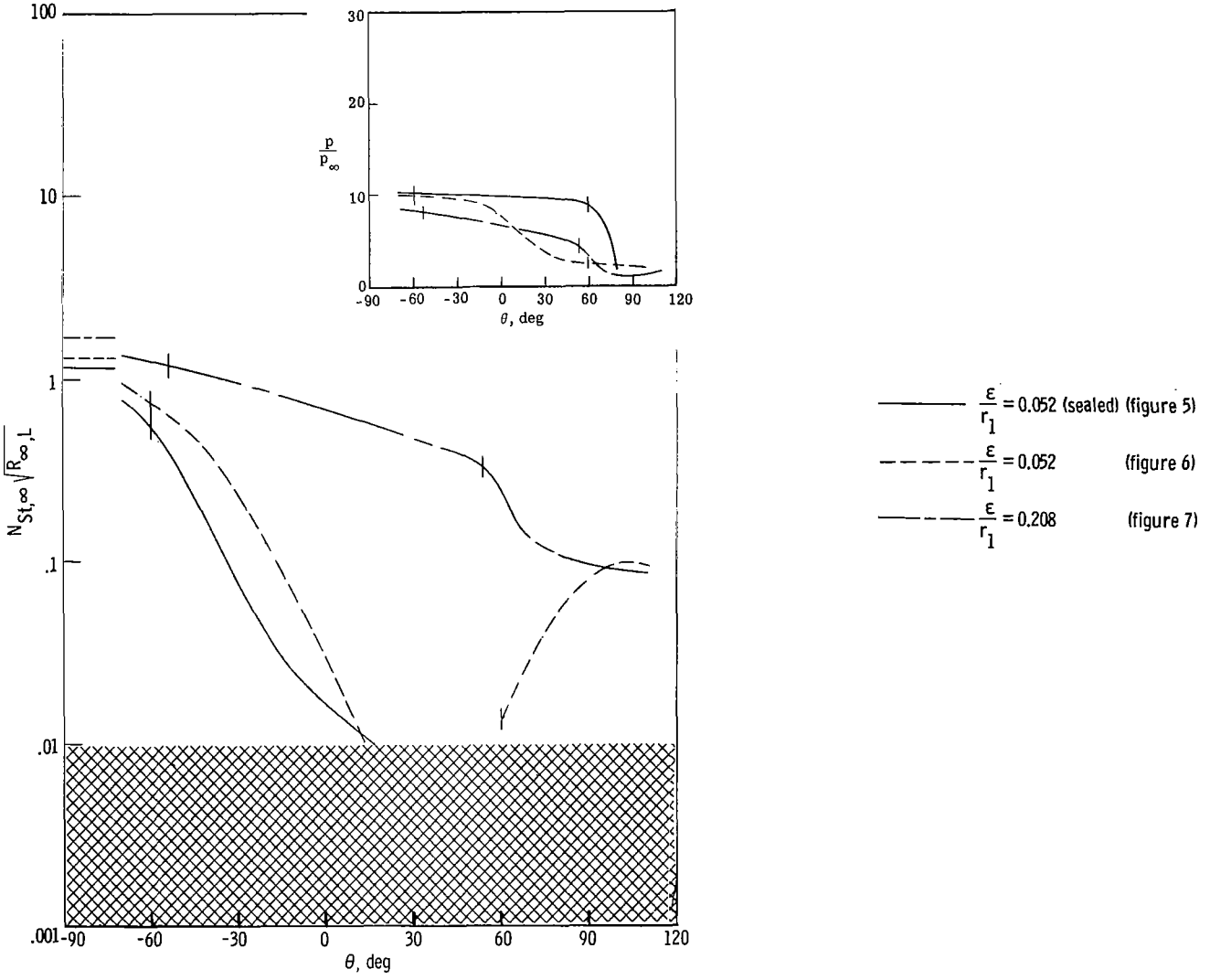

(c) $\delta_f = 20^o$.

Figure 8.- Effect of gap size on pressure and heat transfer for the sharp-entrance gap at $\alpha = 6.83^o$ and $R_{\infty,L} = 0.8 \times 10^6$. $R_{l,L} = 1.18 \times 10^6$; $M_l = 7.7$.

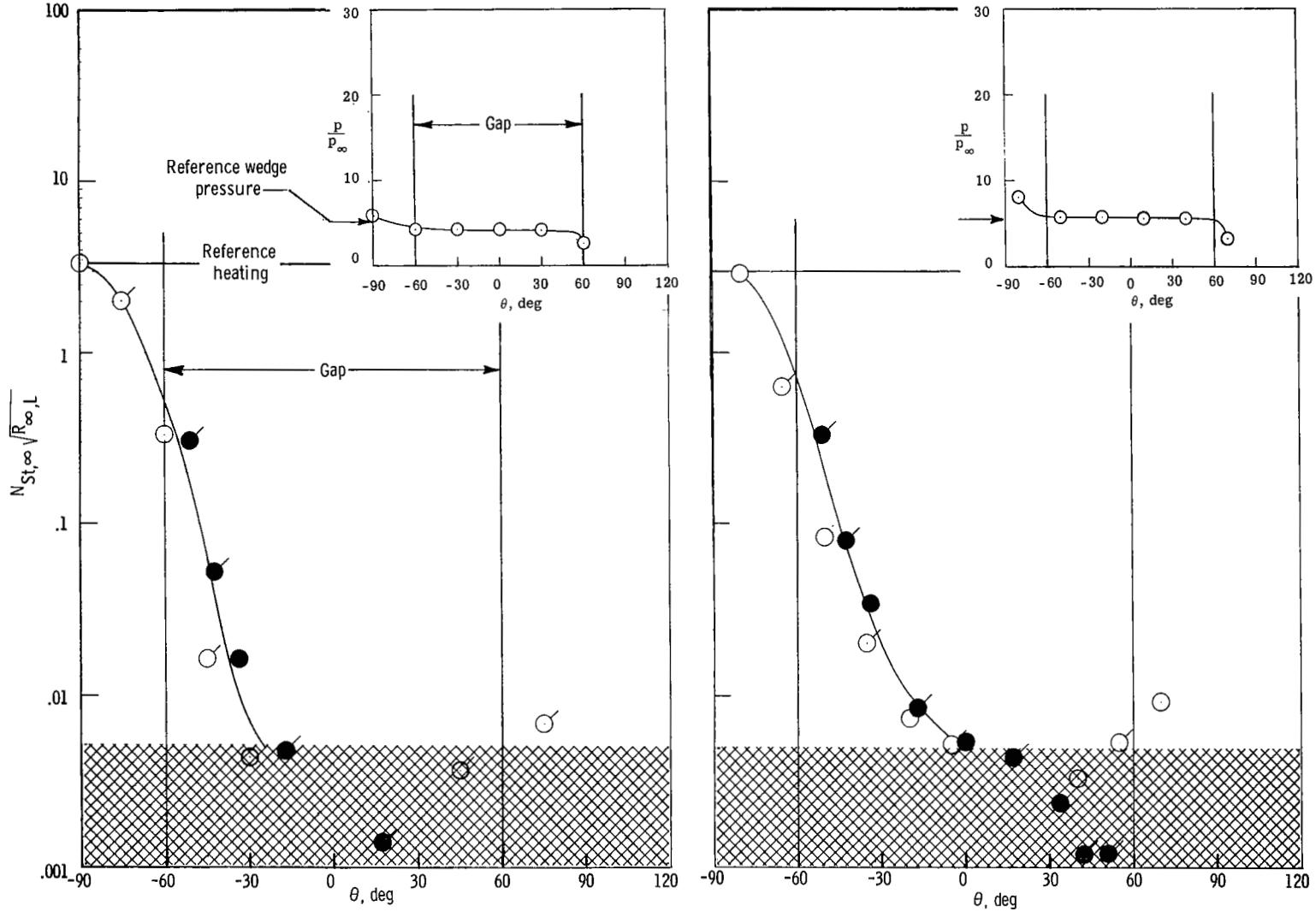

(a) $\delta_f = 0^0$.

(b) $\delta_f = 10^0$.

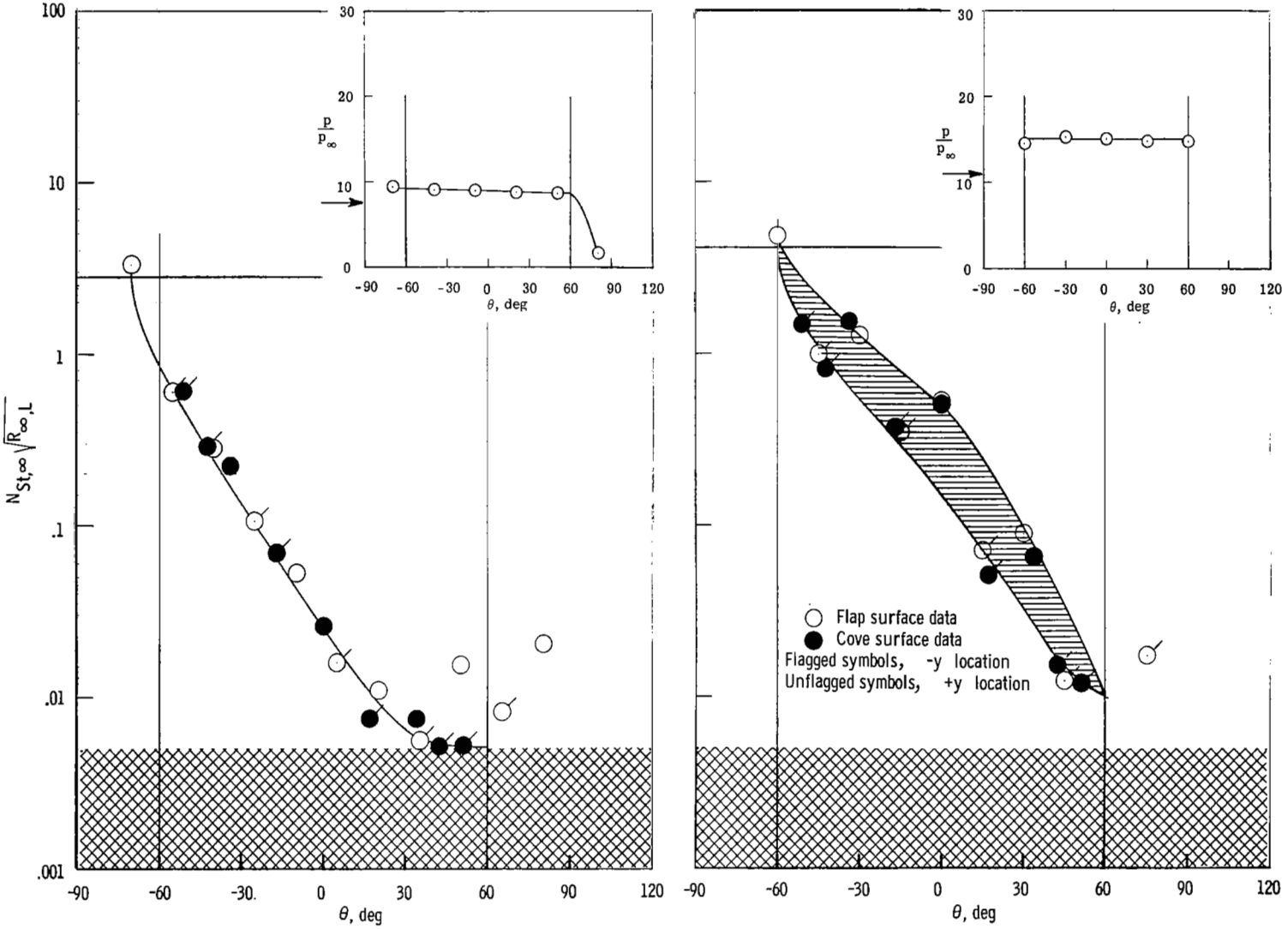

(c) $\delta_f = 20^0$.

(d) $\delta_f = 30^0$.

Figure 9.- Pressure and heat-transfer distributions in the sealed, sharp-entrance gap for $\epsilon/r_1 = 0.052$, $R_{\infty,L} = 3.6 \times 10^6$, and $\alpha = 6.83^0$. $R_{l,L} = 5.3 \times 10^6$; $M_l = 7.9$.

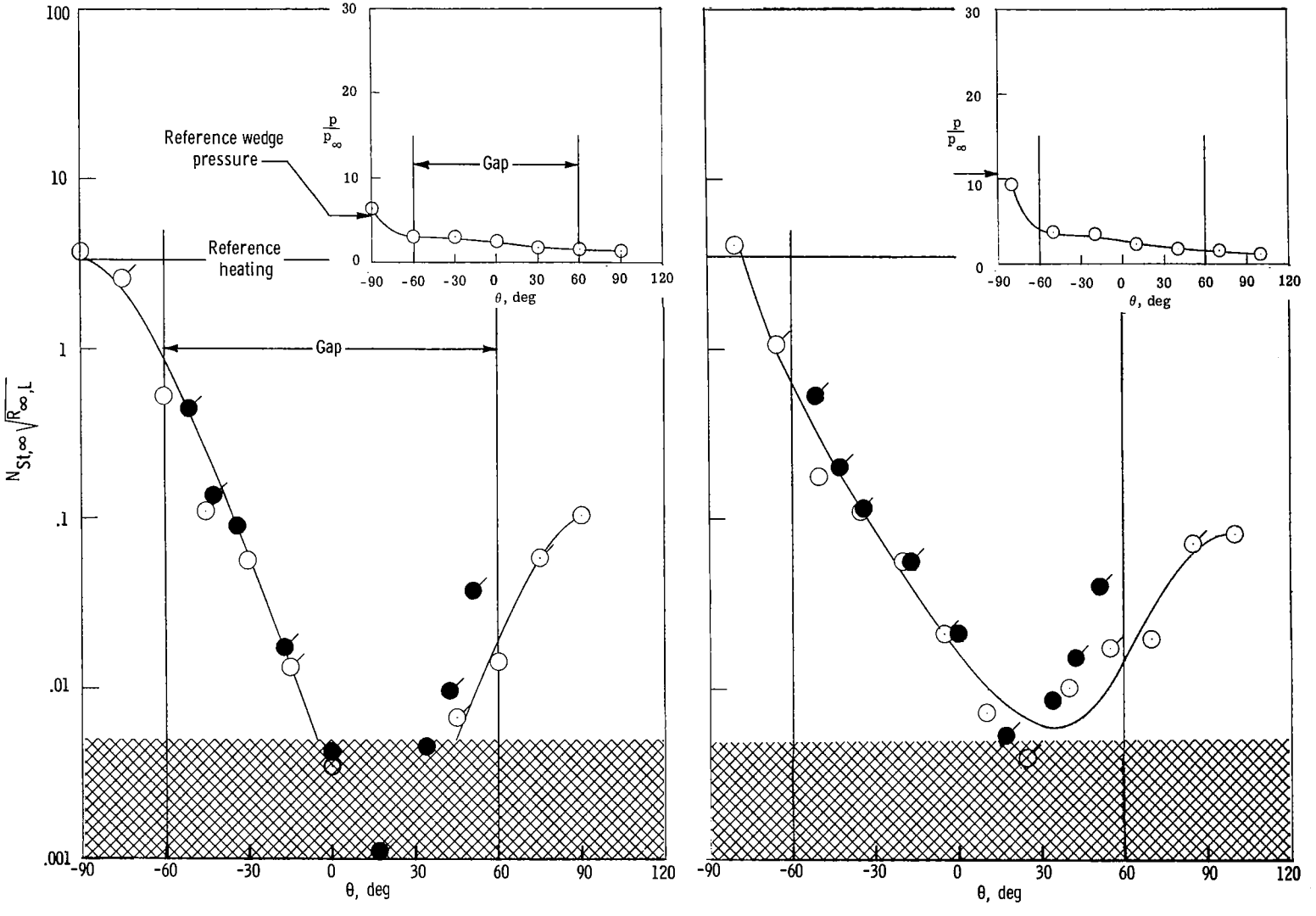

(a) $\delta_f = 0^0$.

(b) $\delta_f = 10^0$.

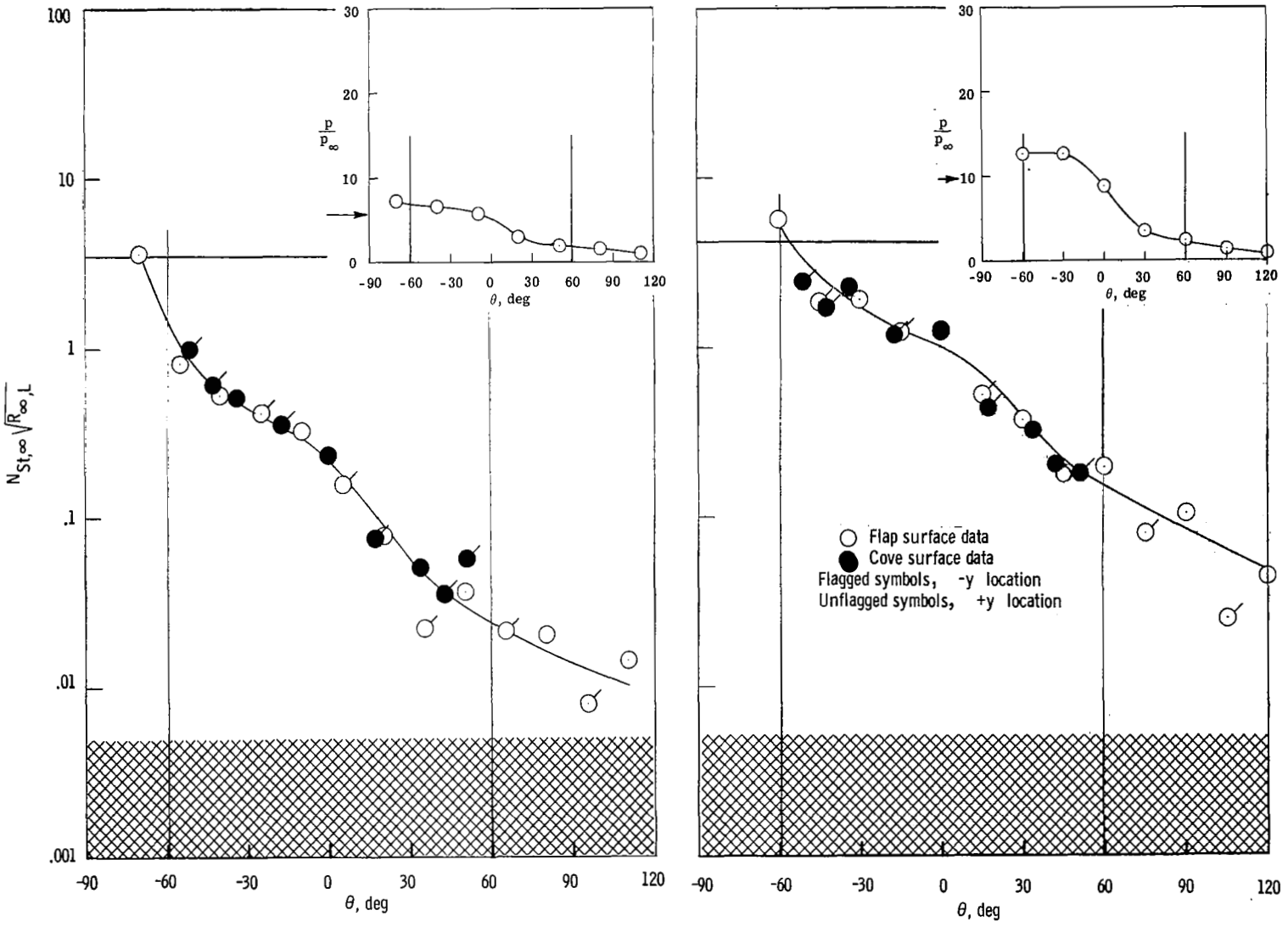

(c) $\delta_f = 20^0$.

(d) $\delta_f = 30^0$.

Figure 10.- Pressure and heat-transfer distributions in the open, sharp-entrance gap for $\varepsilon/r_1 = 0.052$, $R_{\infty,L} = 3.6 \times 10^6$, and $\alpha = 6.83^0$. $R_{\ell,L} = 5.3 \times 10^6$; $M_\ell = 7.9$.

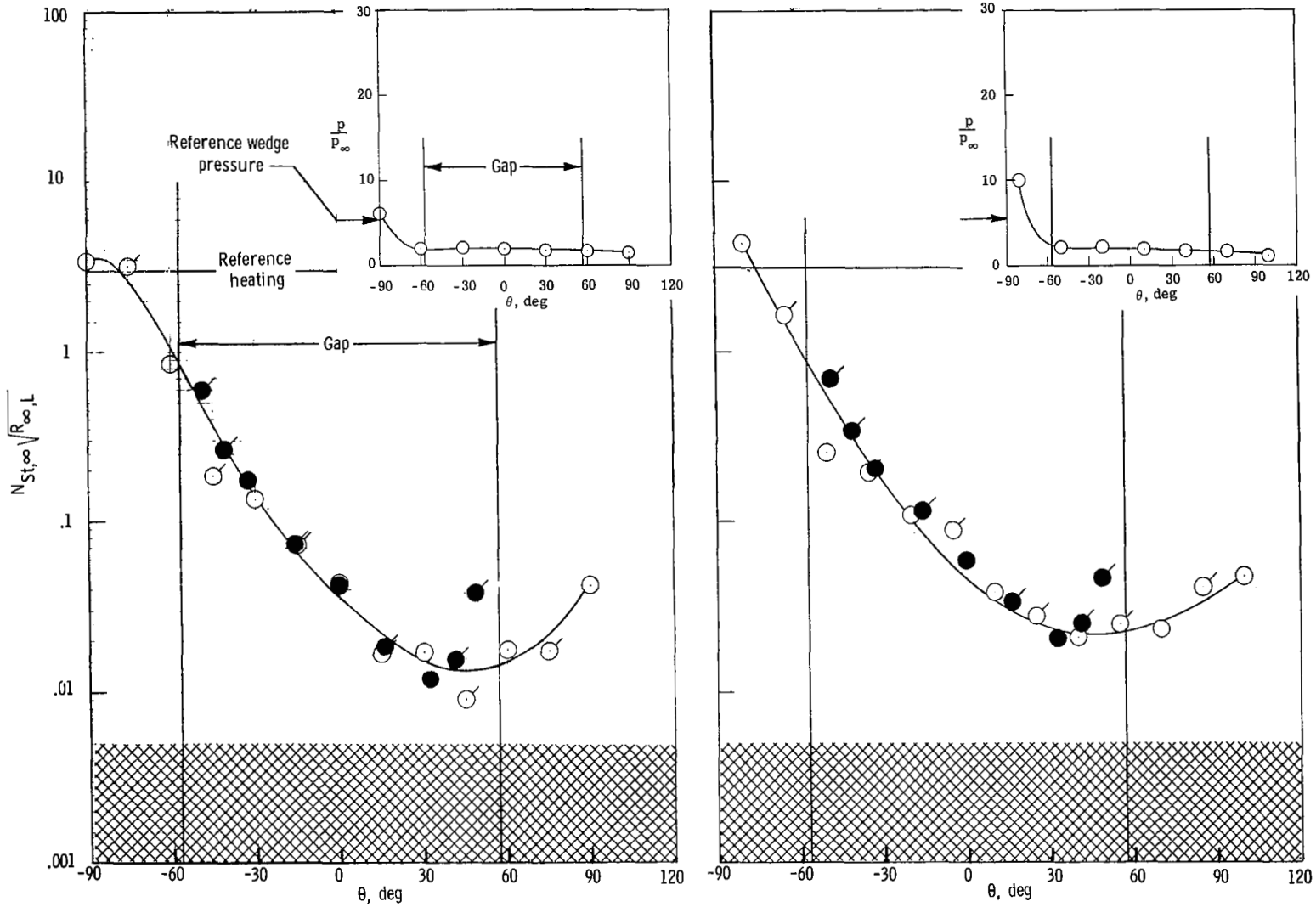

(a) $\delta_f = 0^o$.

(b) $\delta_f = 10^o$.

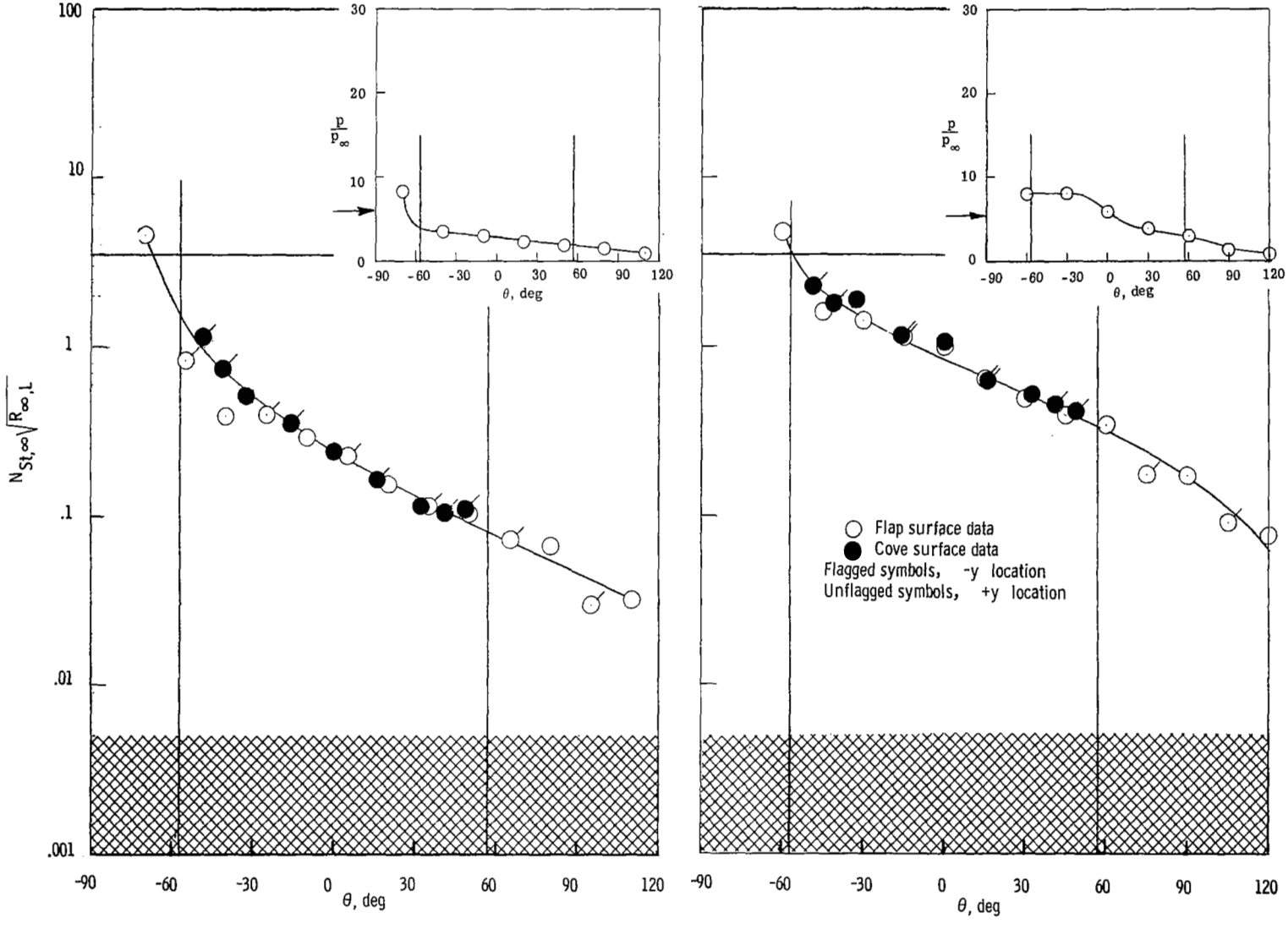

(c) $\delta_f = 20^0$.

(d) $\delta_f = 30^0$.

Figure 11.- Pressure and heat-transfer distributions in the open, sharp-entrance gap for $\varepsilon/r_l = 0.104$, $R_{\infty,L} = 3.6 \times 10^6$, and $\alpha = 6.83^0$. $R_{l,L} = 5.3 \times 10^6$; $M_l = 7.9$.

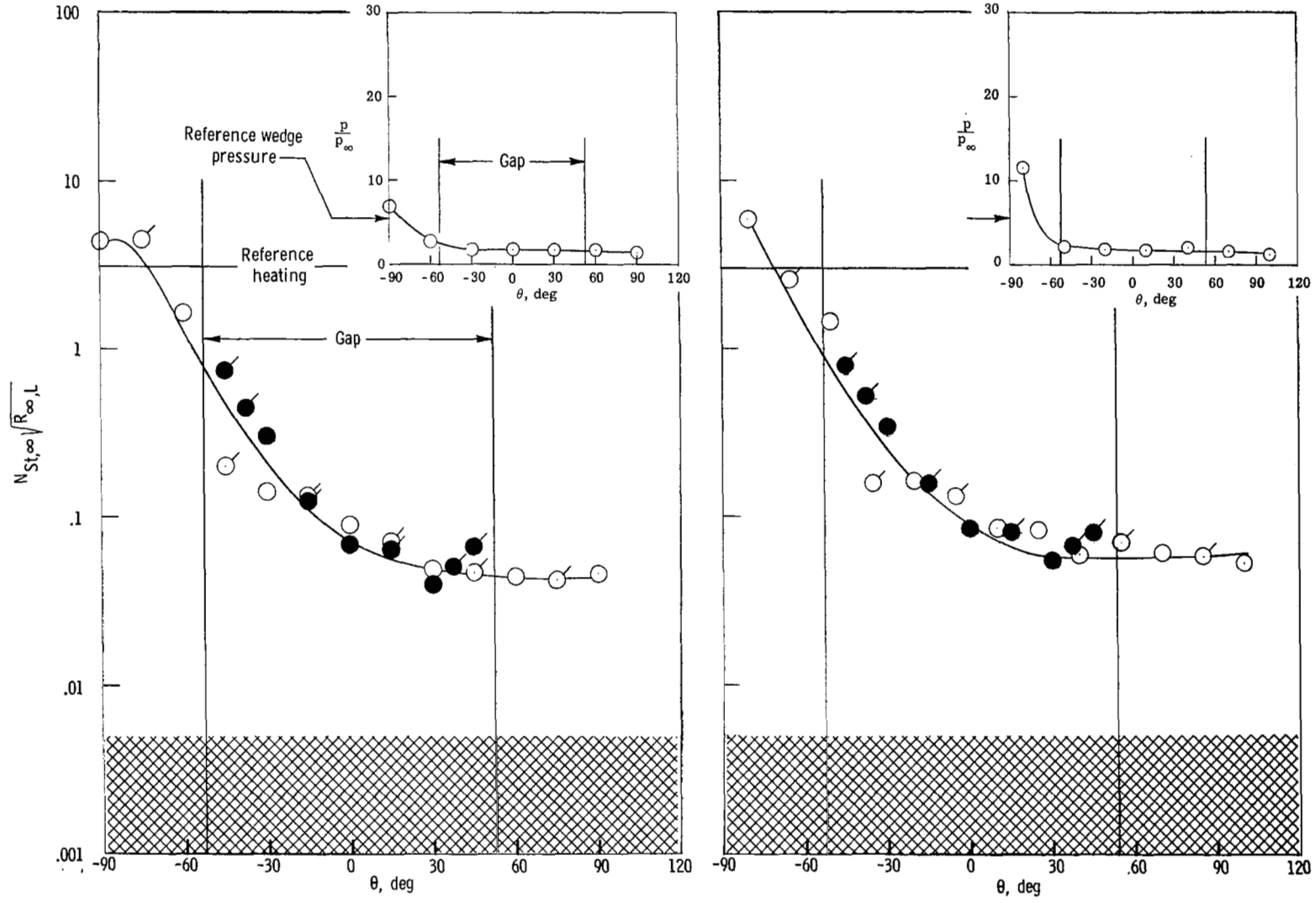

(a) $\delta_f = 0^o$.

(b) $\delta_f = 10^o$.

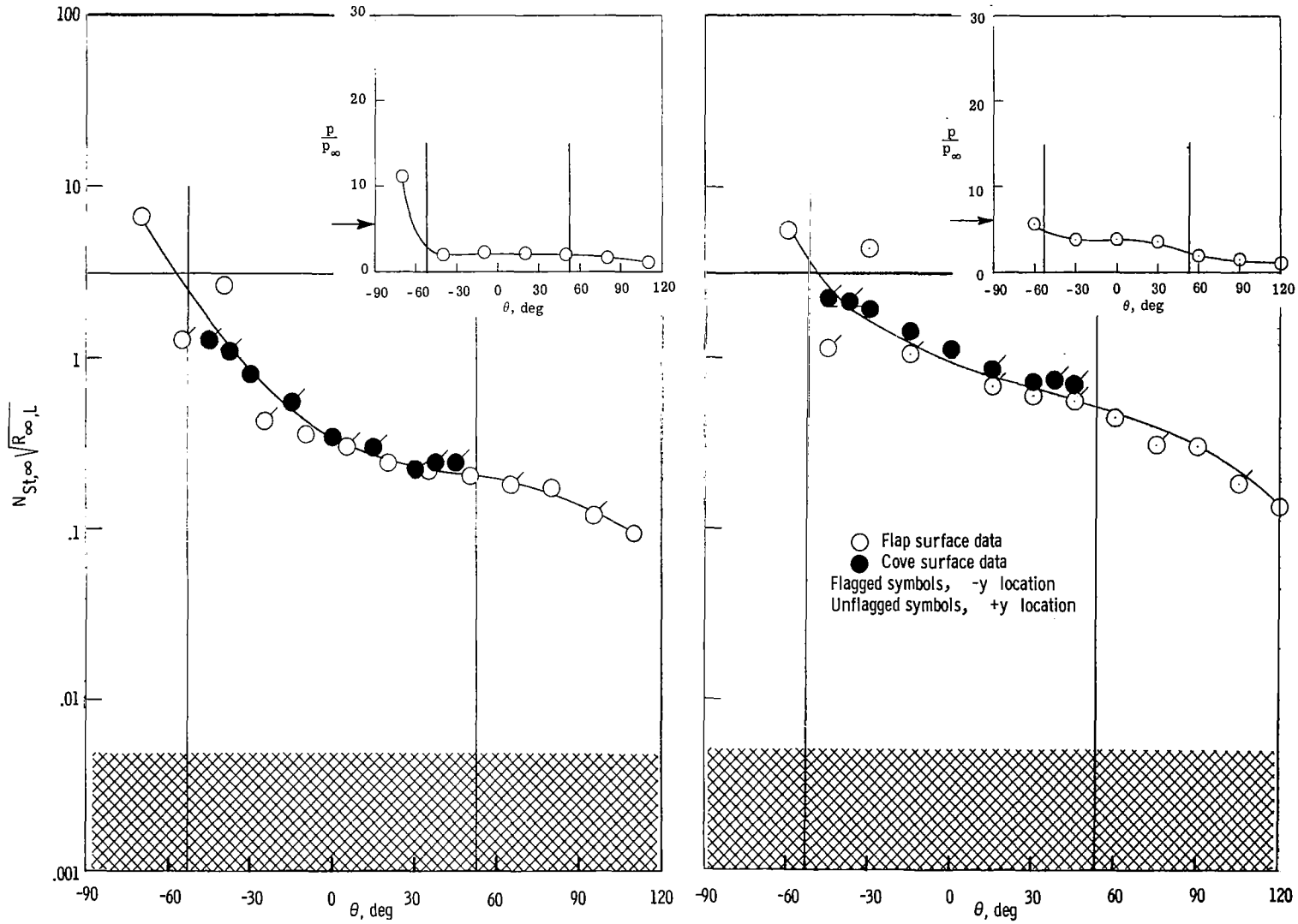

(c) $\delta_f = 20^0$.

(d) $\delta_f = 30^0$.

Figure 12.- Pressure and heat-transfer distributions in the open, sharp-entrance gap for $\varepsilon/r_1 = 0.208$, $R_{\infty,L} = 3.6 \times 10^6$, and $\alpha = 6.83^0$. $R_{\ell,L} = 5.3 \times 10^6$; $M_\ell = 7.9$.

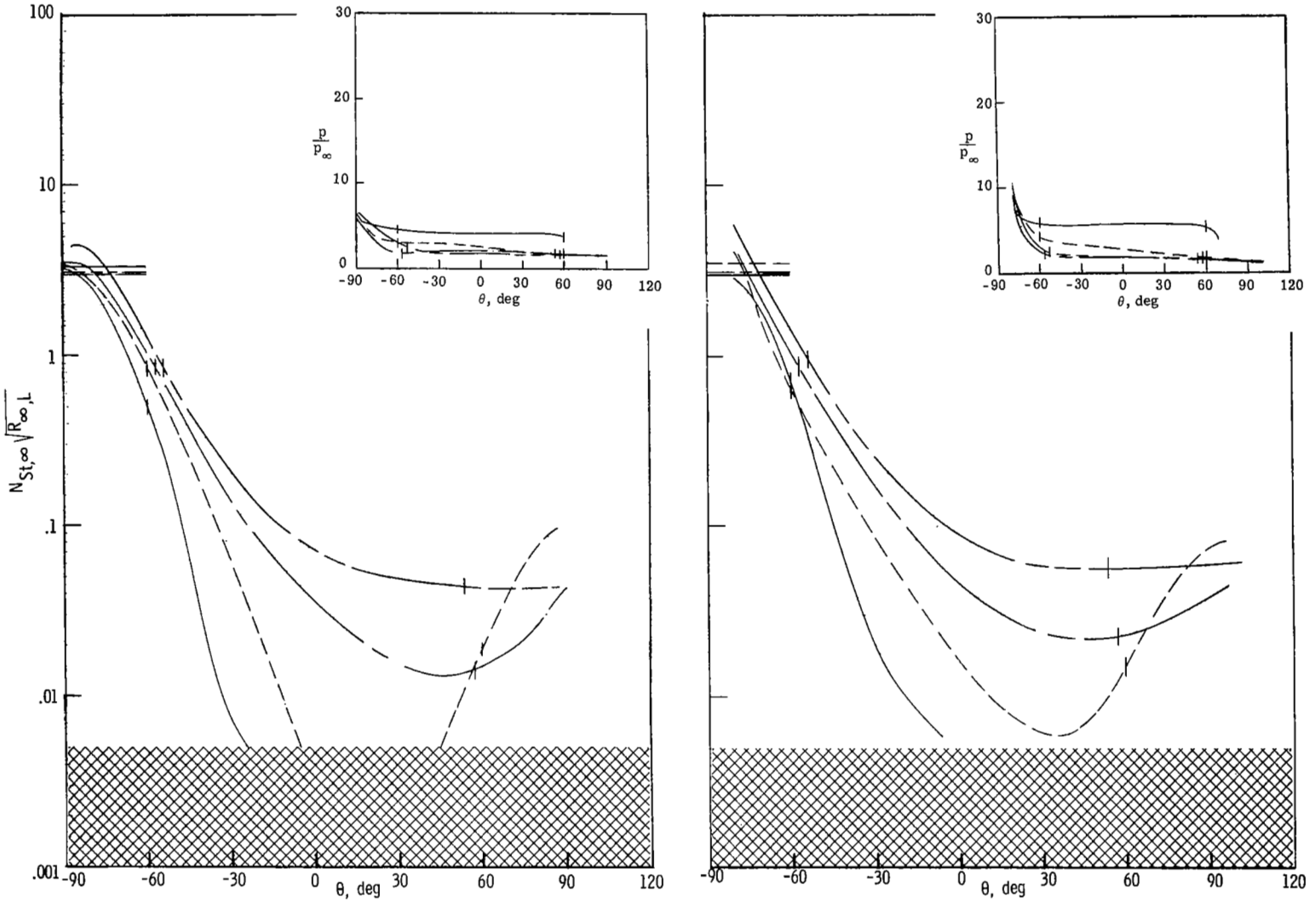

(a) $\delta_f = 0^o$.

(b) $\delta_f = 10^o$.

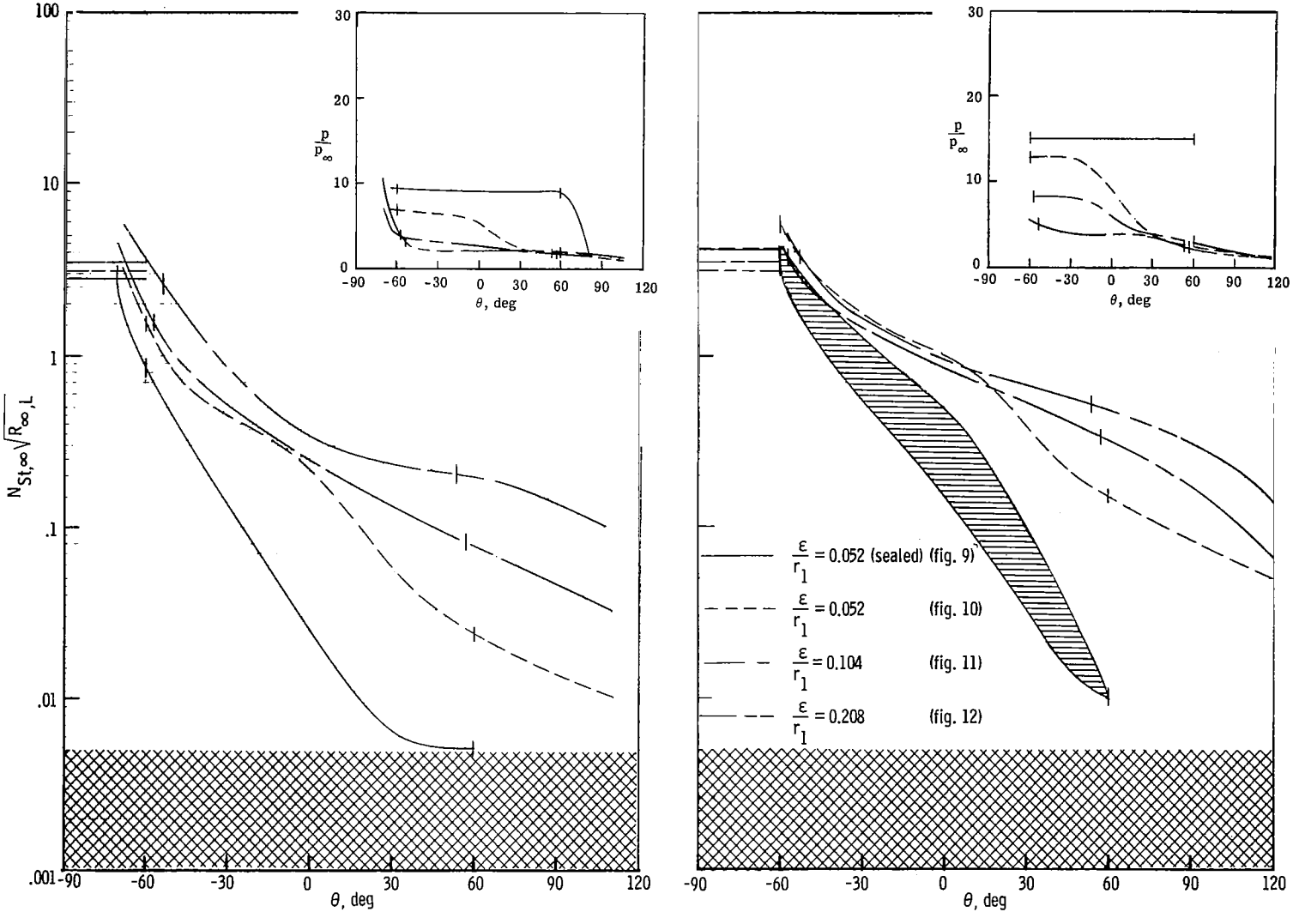

(c) $\delta_f = 20^0$.

(d) $\delta_f = 30^0$.

Figure 13.- Effect of gap size on the pressure and heat transfer in the sharp-entrance gap at $\alpha = 6.83^0$ and $R_{\infty,L} = 3.6 \times 10^6$. $R_{l,L} = 5.3 \times 10^6$; $M_l = 7.9$.

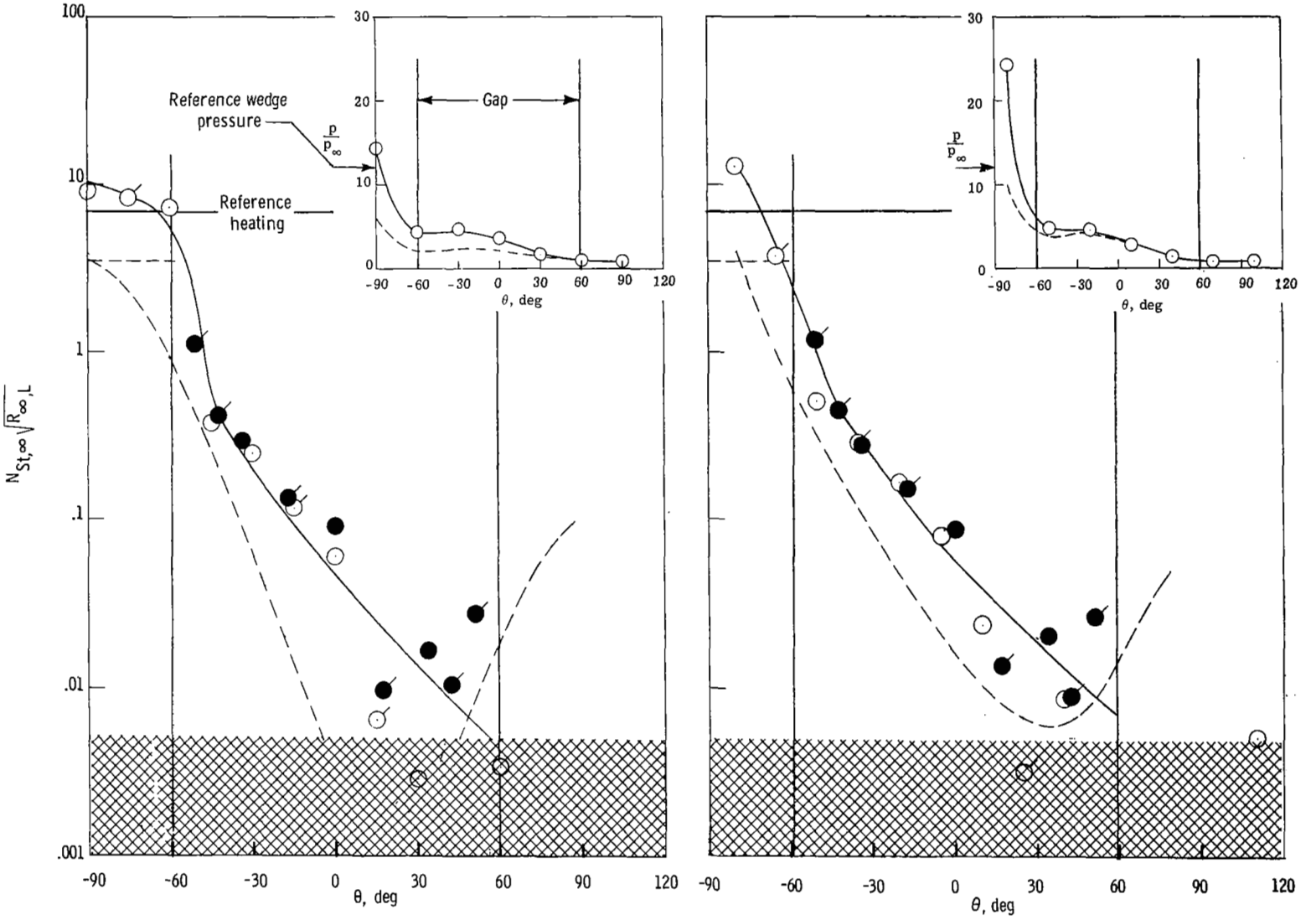

(a) $\delta_f = 0^0$.

(b) $\delta_f = 10^0$.

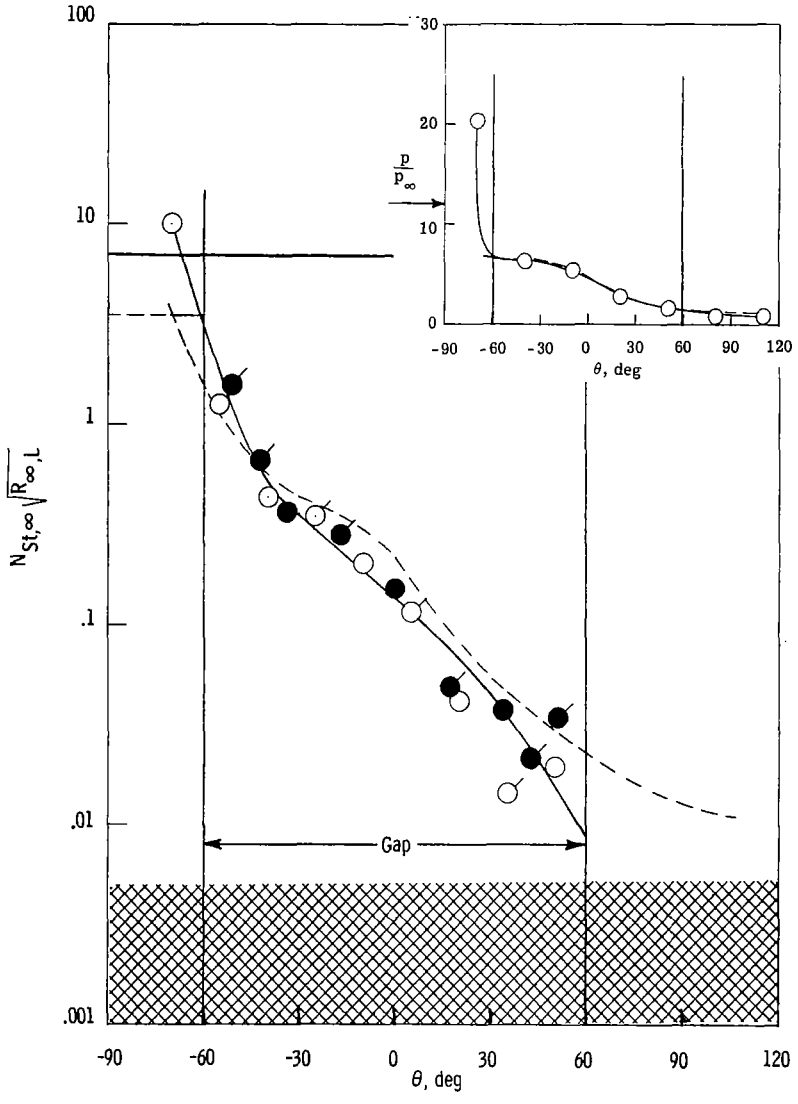

○ Flap surface data
● Cove surface data
Flagged symbols, -y location
Unflagged symbols, +y location
– – – Same gap at $\alpha = 6.83^0$ (fig. 10)

(c) $\delta_f = 20^0$.

Figure 14.- Effect of increasing the entrance-to-exit pressure ratio on the pressure and heat transfer in the open, sharp-entrance gap for $\varepsilon/r_1 = 0.052$, $R_{\infty,L} = 3.6 \times 10^6$, and $\alpha = 12.83^0$. $R_{\ell,L} = 4.5 \times 10^6$; $M_\ell = 5.9$.

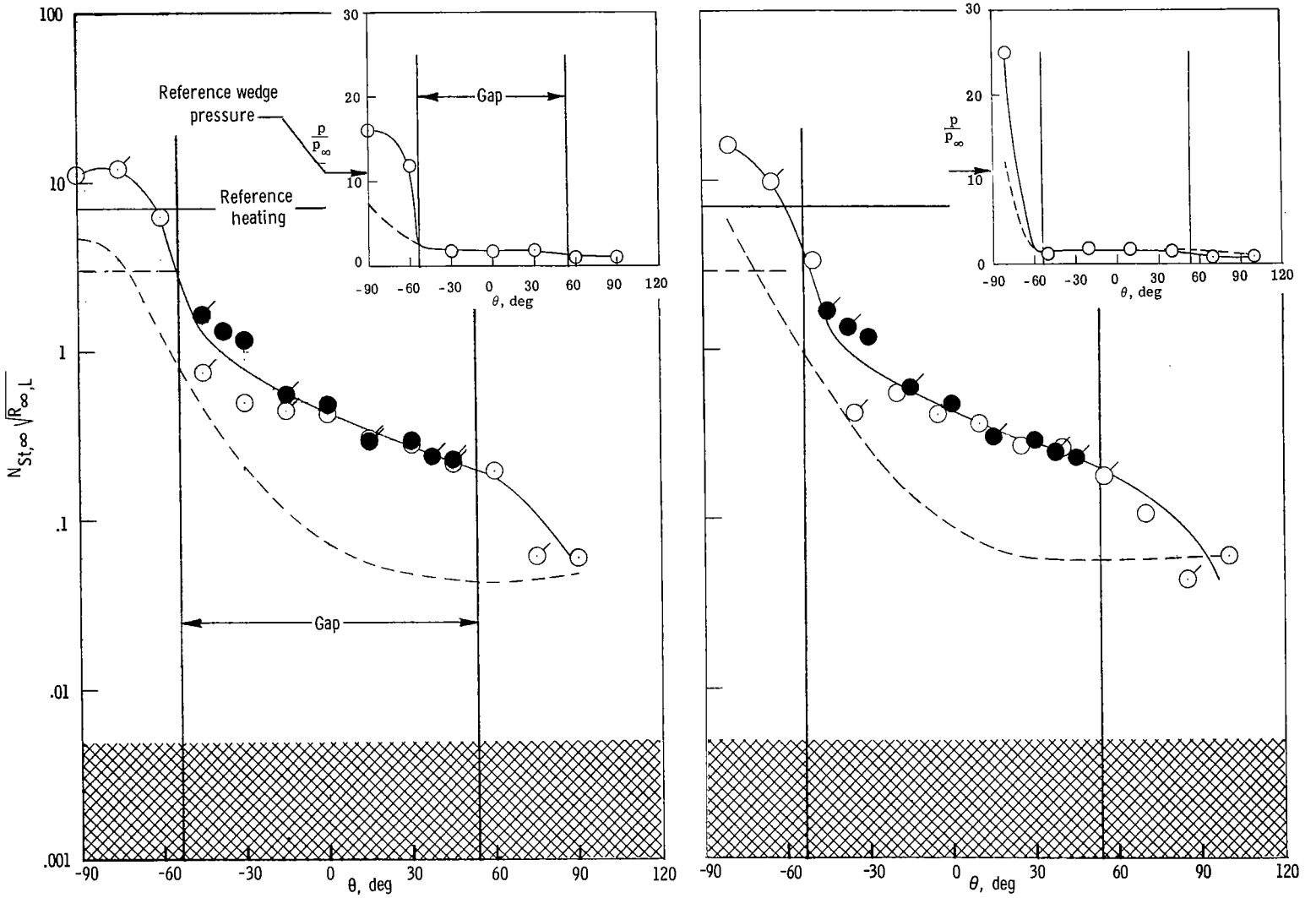

(a) $\delta_f = 0^0$.

(b) $\delta_f = 10^0$.

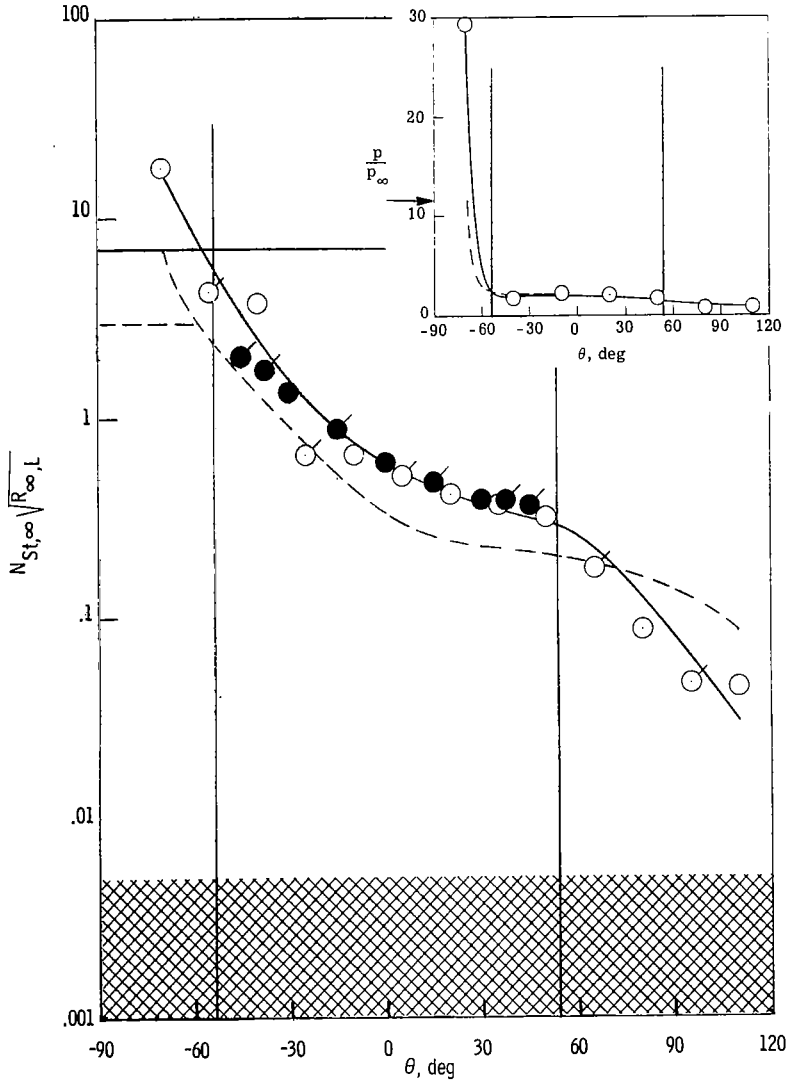

○ Flap surface data
● Cove surface data
Flagged symbols, -y location
Unflagged symbols, +y location
– – – Same gap at $\alpha = 6.83^0$ (fig. 12)

(c) $\delta_f = 20^0$.

Figure 15.- Effect of increasing the entrance-to-exit pressure ratio on the pressure and heat transfer in the open, sharp-entrance gap for $\varepsilon/r_1 = 0.208$, $R_{\infty,L} = 3.6 \times 10^6$, and $\alpha = 12.83^0$. $R_{l,L} = 4.5 \times 10^6$; $M_l = 5.9$.

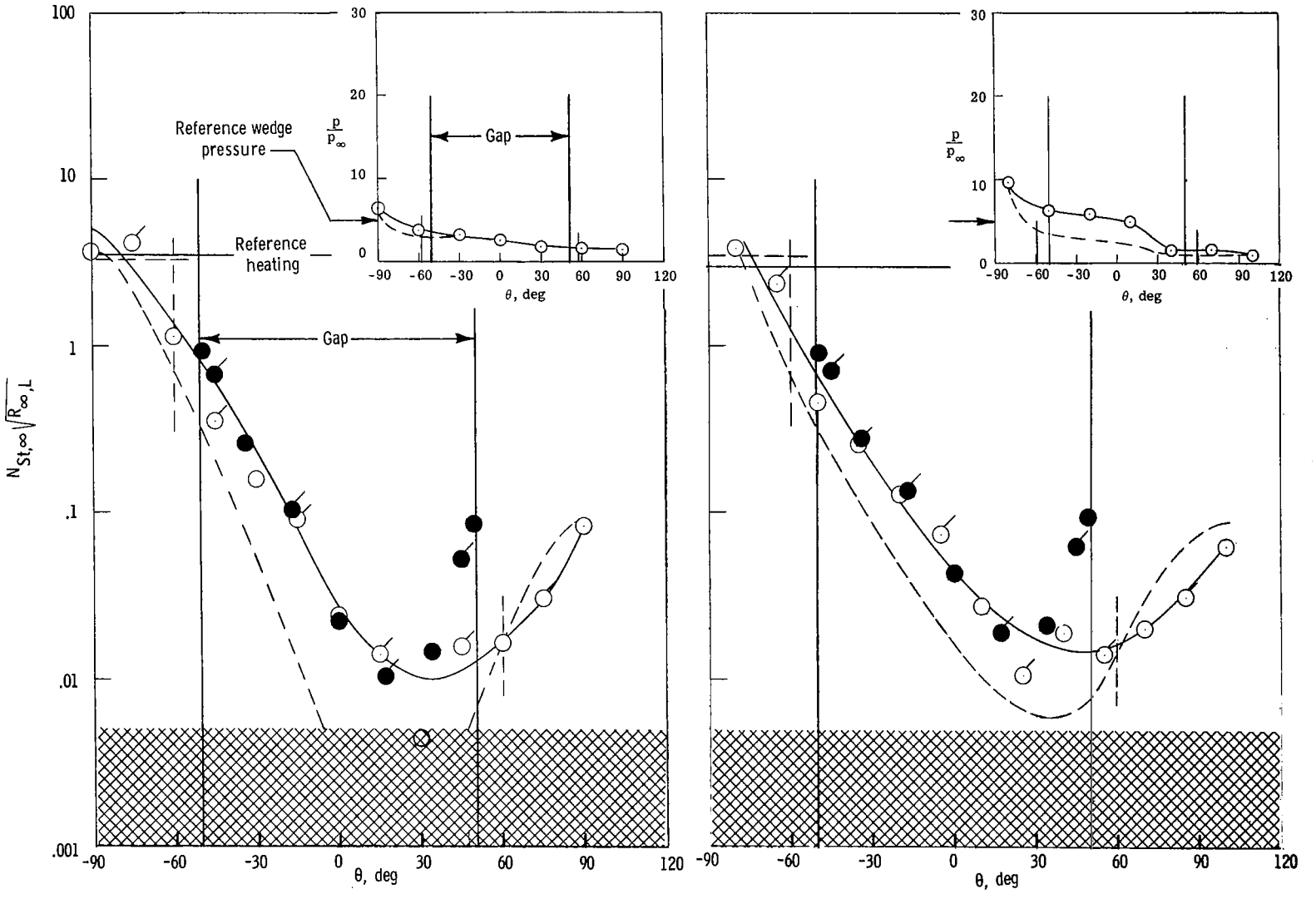

(a) $\delta_f = 0^0$.

(b) $\delta_f = 10^0$.

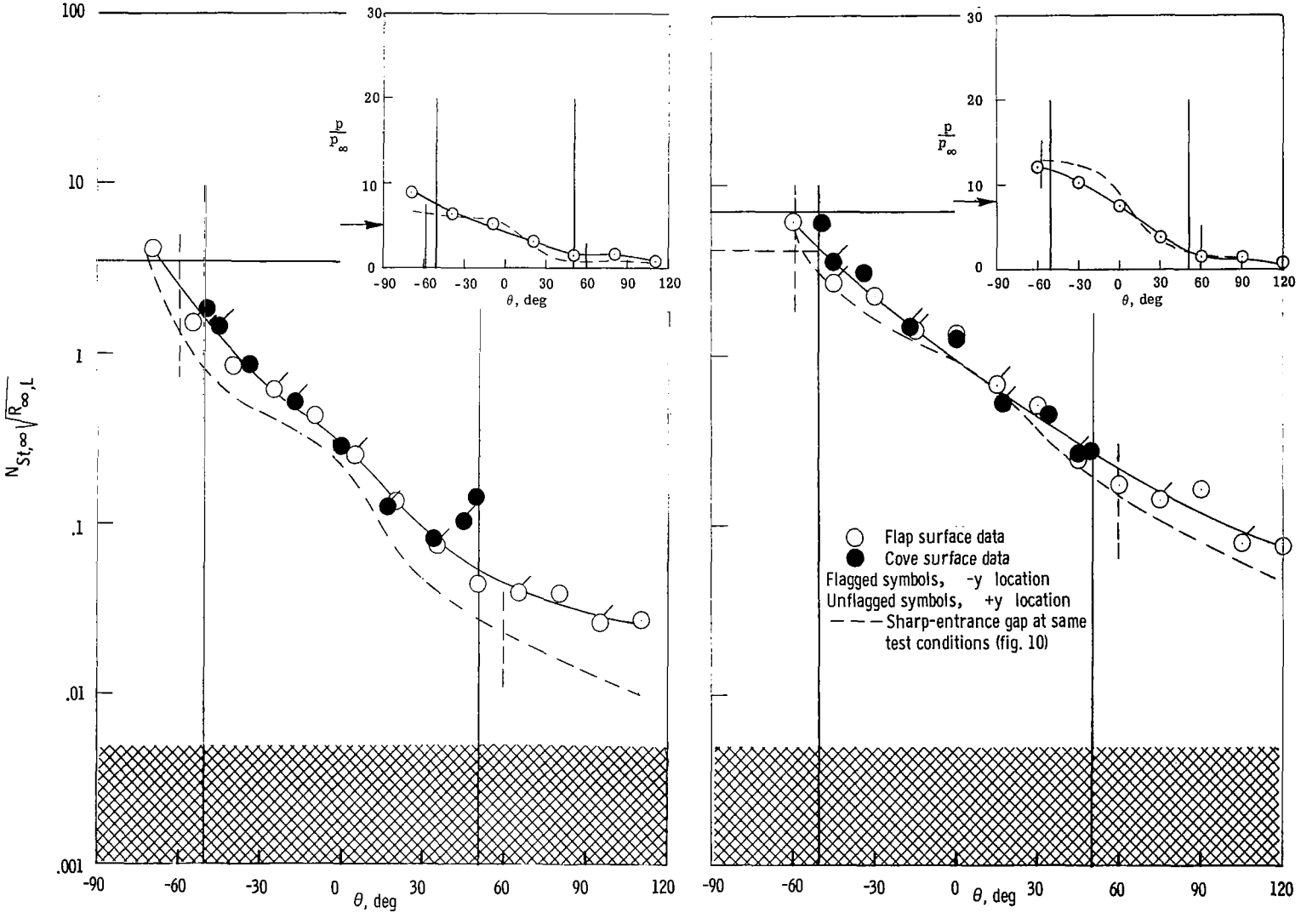

(c) $\delta_f = 20^0$.

(d) $\delta_f = 30^0$.

Figure 16.- Effect of the entrance geometry on the pressure and heat transfer in the open, rounded-entrance gap with $\varepsilon/r_1 = 0.052$, $R_{\infty,L} = 3.6 \times 10^6$, and $\alpha = 6.83^0$. $R_{l,L} = 5.3 \times 10^6$; $M_l = 7.9$.

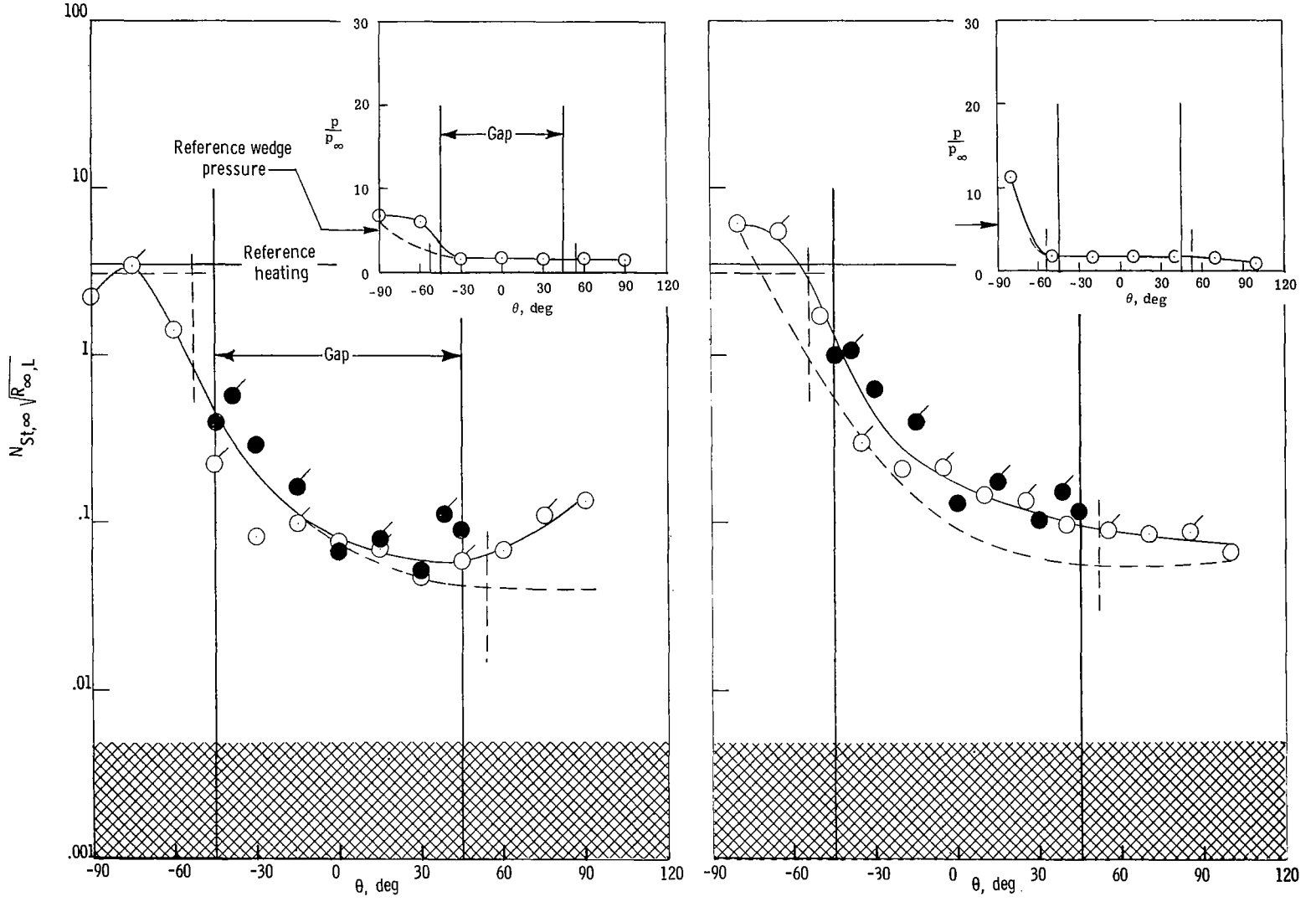

(a) $\delta_f = 0^o$.

(b) $\delta_f = 10^o$.

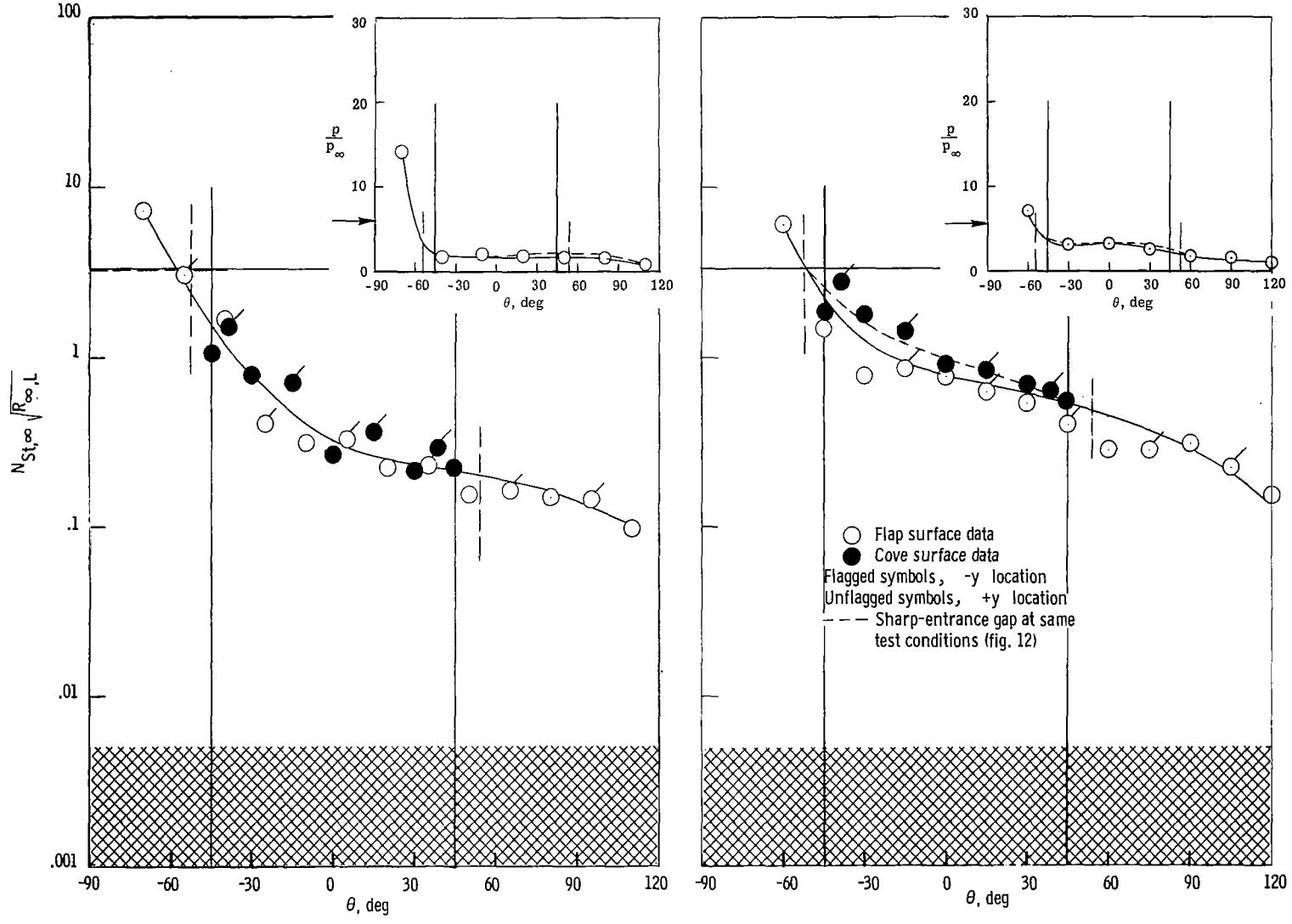

(c) $\delta_f = 20^o$.

(d) $\delta_f = 30^o$.

Figure 17.- Effect of entrance geometry on the pressure and heat transfer in the open, rounded-entrance gap with $\varepsilon/r_1 = 0.208$, $R_{\infty,L} = 3.6 \times 10^6$, and $\alpha = 6.83^o$. $R_{l,L} = 5.3 \times 10^6$; $M_l = 7.9$.

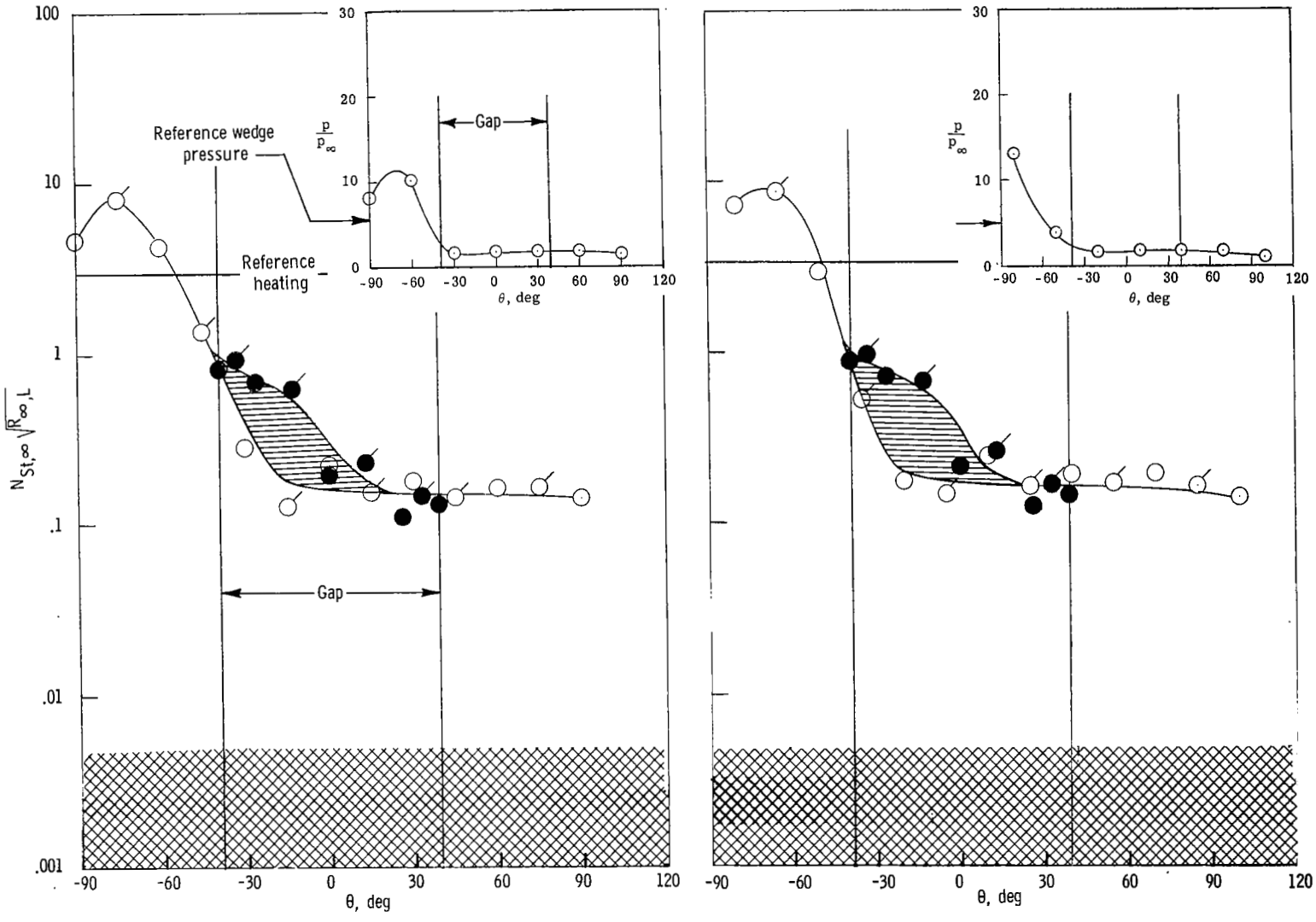

(a) $\delta_f = 0^0$.

(b) $\delta_f = 10^0$.

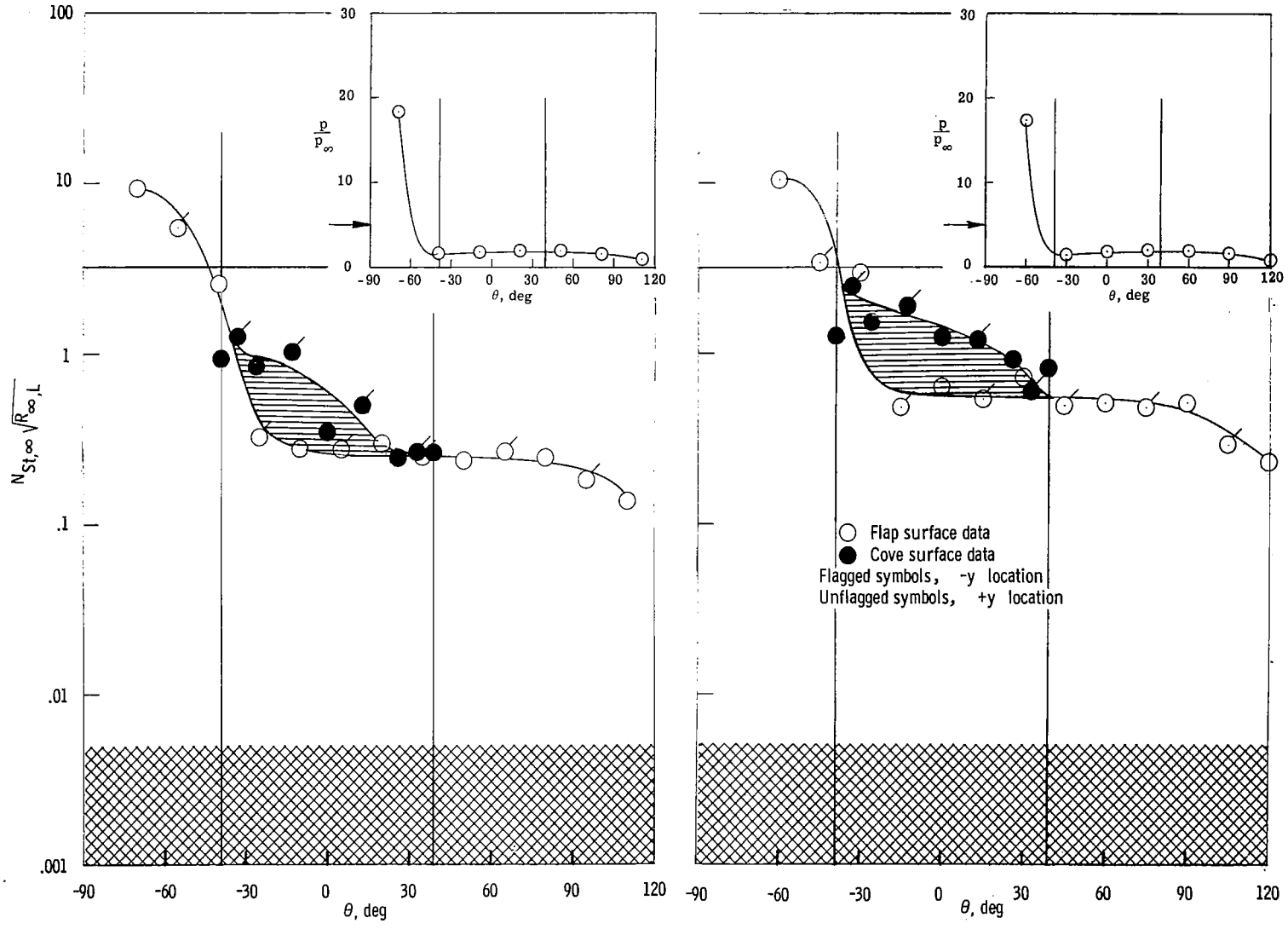

(c) $\delta_f = 20^0$.

(d) $\delta_f = 30^0$.

Figure 18.- Pressure and heat-transfer distributions in the open, rounded-entrance gap for $\varepsilon/r_1 = 0.416$, $R_{\infty,L} = 3.6 \times 10^6$, and $\alpha = 6.83^0$. $R_{l,L} = 5.3 \times 10^6$; $M_l = 7.9$.

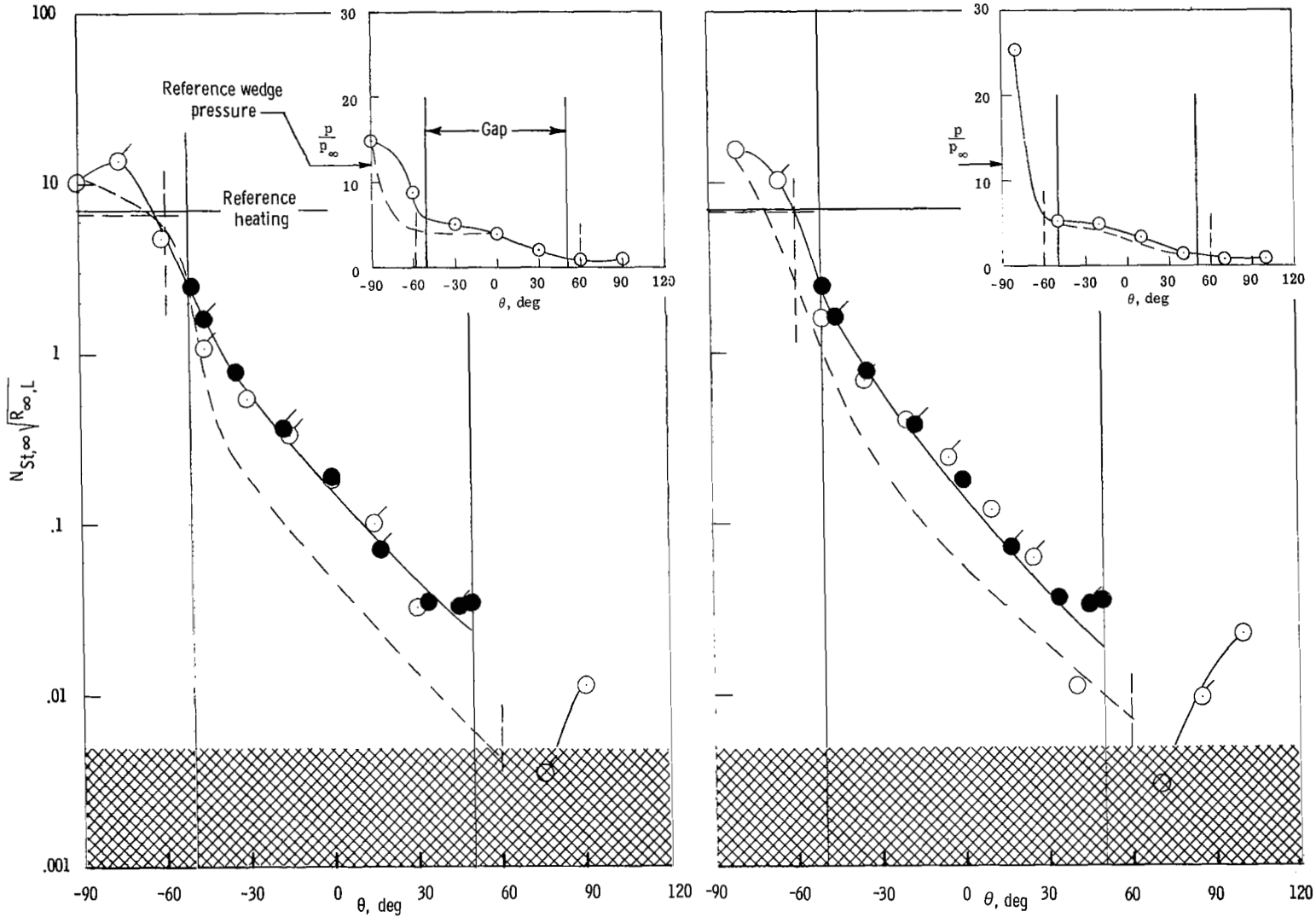

(a) $\delta_f = 0^o$.

(b) $\delta_f = 10^o$.

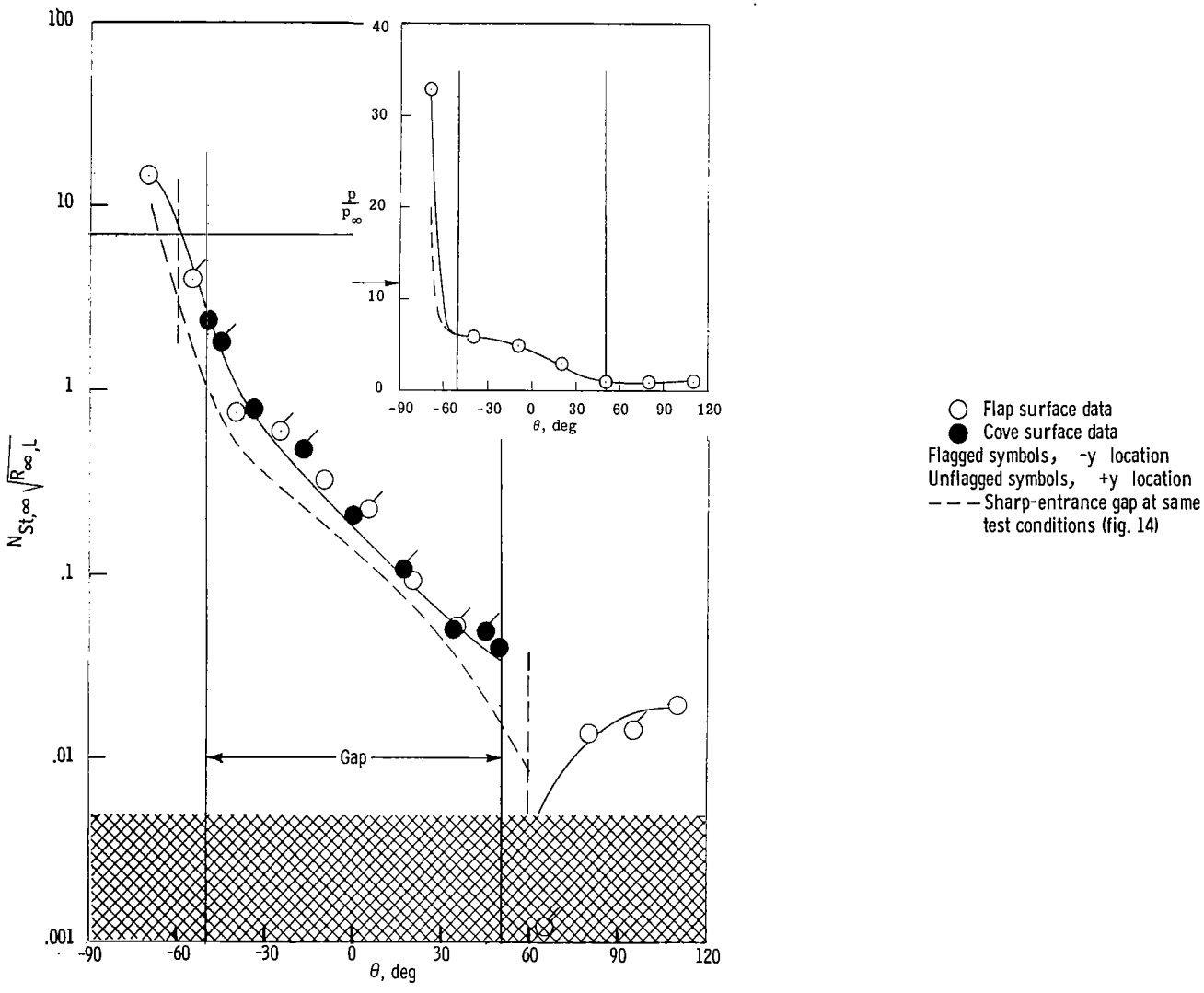

(c) $\delta_f = 20^o$.

Figure 19.- Effect of entrance geometry on the pressure and heat transfer in the open, rounded-entrance gap with $\varepsilon/r_1 = 0.052$, $R_{\infty,L} = 3.6 \times 10^6$, and $\alpha = 12.83^o$. $R_{l,L} = 4.5 \times 10^6$; $M_l = 5.9$.

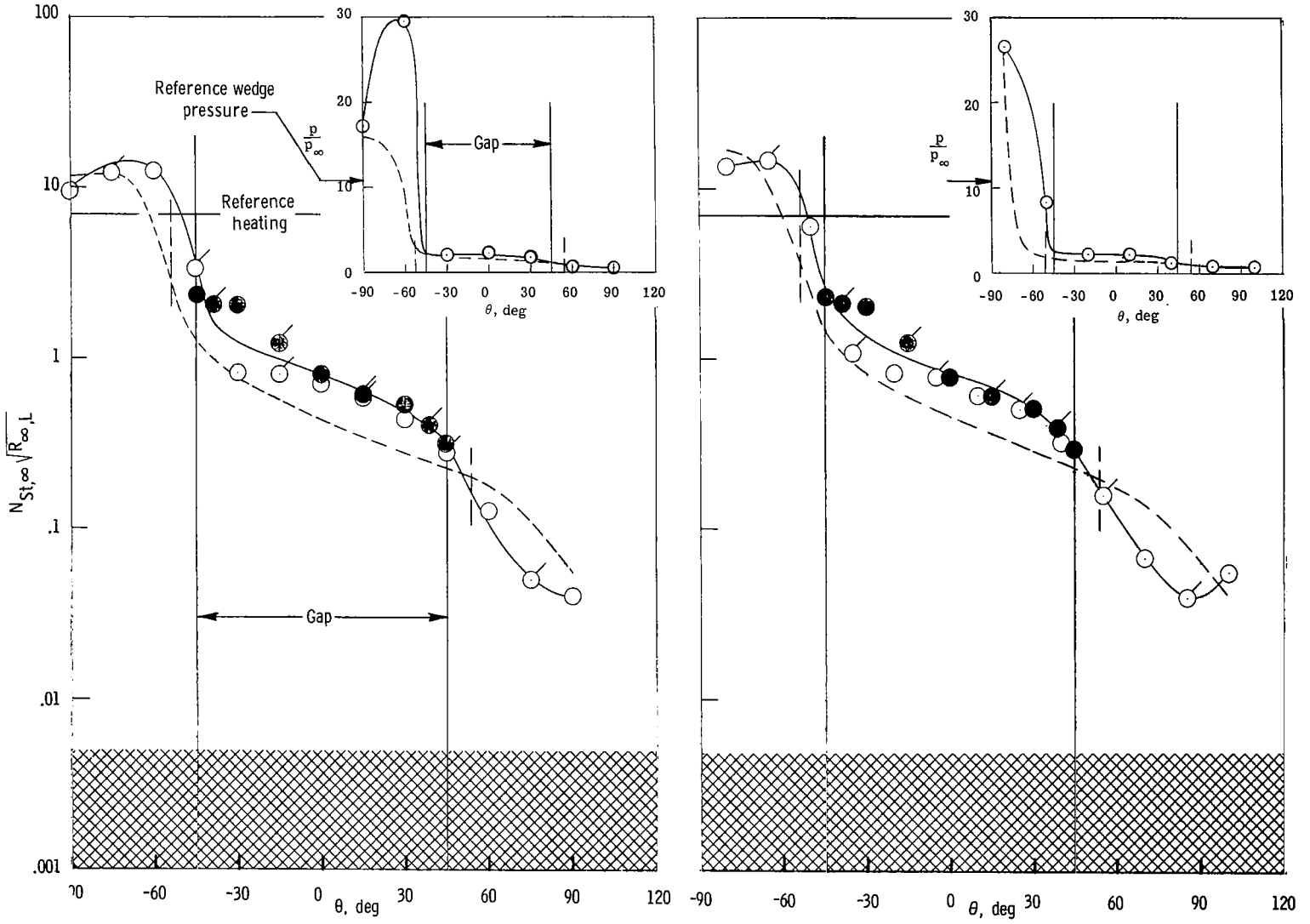

(a) $\delta_f = 0^o$.

(b) $\delta_f = 10^o$.

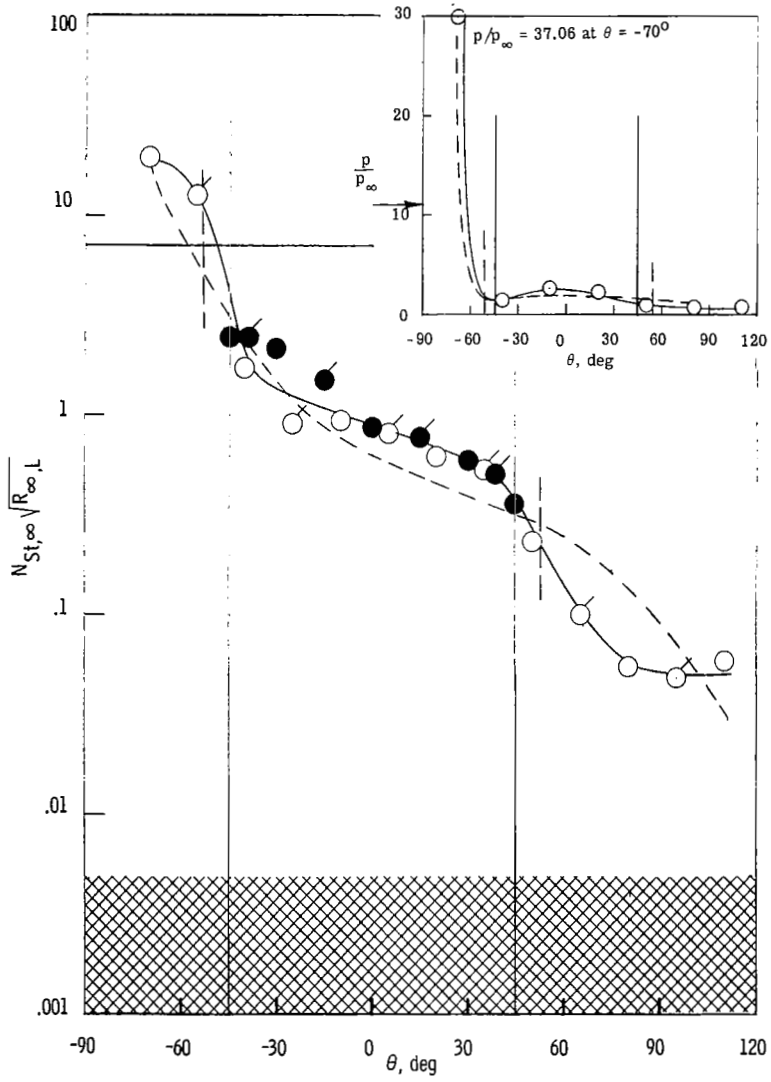

○ Flap surface data
● Cove surface data
Flagged symbols, -y location
Unflagged symbols, +y location
– – – Sharp-entrance gap at the same test conditions (fig. 15)

(c) $\delta_f = 20^0$.

Figure 20.- Effect of entrance geometry on the pressure and heat transfer in the open, rounded-entrance gap with $\varepsilon/r_1 = 0.208$, $R_{\infty,L} = 3.6 \times 10^6$, and $\alpha = 12.83^0$. $R_{l,L} = 4.5 \times 10^6$; $M_l = 5.9$.

(a) $\delta_f = 0^o$.

(b) $\delta_f = 10^o$.

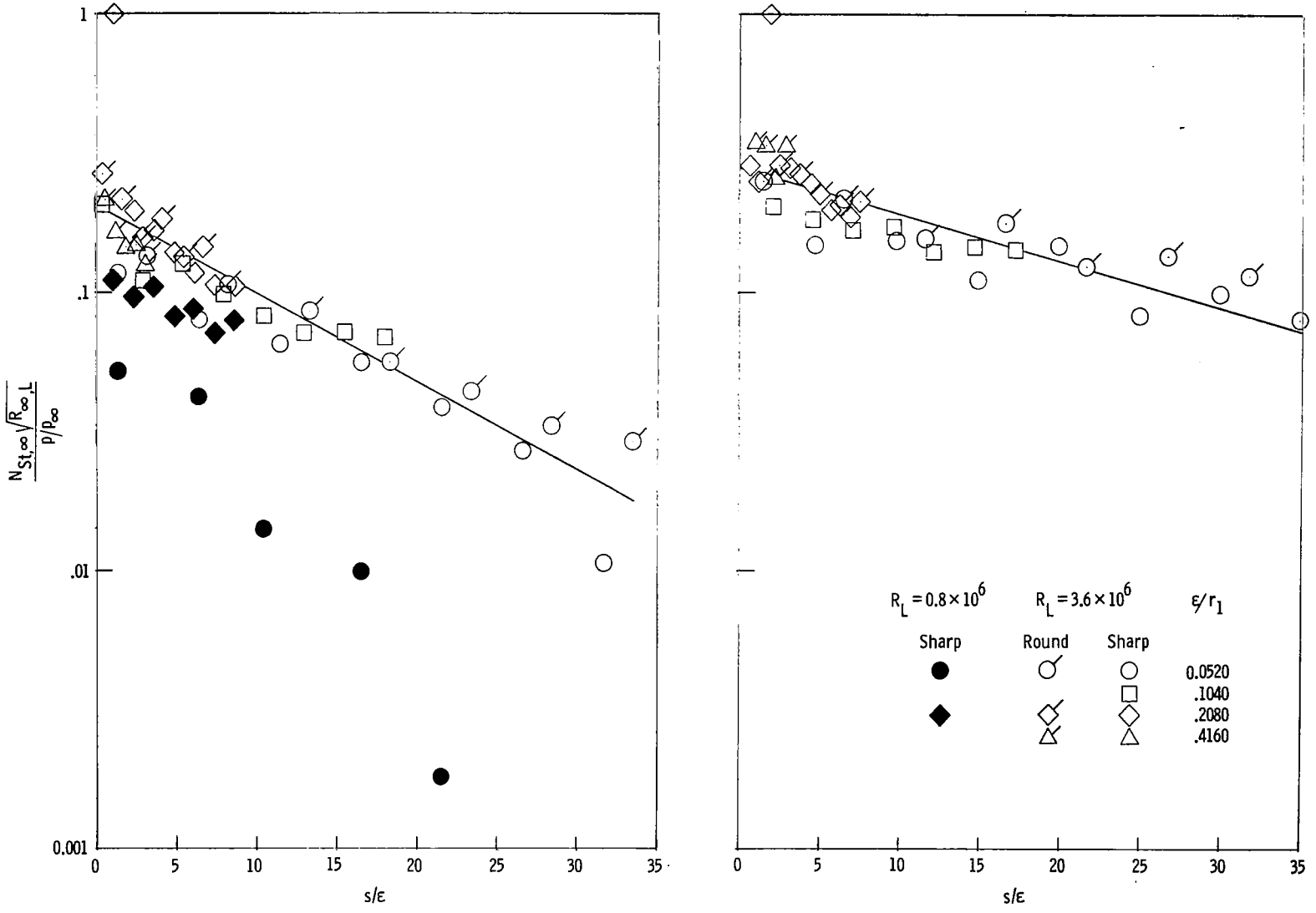

(c) $\delta_f = 20^0$.

(d) $\delta_f = 30^0$.

Figure 21.- Correlation of gap heating data for $\alpha = 6.83^0$.